Article

An aberrant immune–epithelial progenitor niche drives viral lung sequelae

Harish Narasimhan[1,2,3,16], In Su Cheon[1,2,16], Wei Qian[1,2,16], Sheng'en Shawn Hu[4,16], Tanyalak Parimon[5,6,16], Chaofan Li[1,2], Nick Goplen[7], Yue Wu[1,2], Xiaoqin Wei[1,2], Young Min Son[8], Elizabeth Fink[1,2], Gislane de Almeida Santos[1,2], Jinyi Tang[1,2], Changfu Yao[5,6], Lyndsey Muehling[9], Glenda Canderan[9], Alexandra Kadl[10], Abigail Cannon[1,2], Samuel Young[1,2,3], Riley Hannan[10], Grace Bingham[11], Mohammed Arish[1,2], Arka Sen Chaudhari[1,2], Jun sub Im[1,2], Cameron L. R. Mattingly[12,13], Patcharin Pramoonjago[14], Alberto Marchesvsky[15], Jeffrey Sturek[10], Jacob E. Kohlmeier[12,13], Yun Michael Shim[10], Judith Woodfolk[9], Chongzhi Zang[4✉], Peter Chen[5,6✉] & Jie Sun[1,2,3✉]

The long-term physiological consequences of respiratory viral infections, particularly in the aftermath of the COVID-19 pandemic—termed post-acute sequelae of SARS-CoV-2 (PASC)—are rapidly evolving into a major public health concern[1–3]. While the cellular and molecular aetiologies of these sequelae are poorly defined, increasing evidence implicates abnormal immune responses[3–6] and/or impaired organ recovery[7–9] after infection. However, the precise mechanisms that link these processes in the context of PASC remain unclear. Here, with insights from three cohorts of patients with respiratory PASC, we established a mouse model of post-viral lung disease and identified an aberrant immune–epithelial progenitor niche unique to fibroproliferation in respiratory PASC. Using spatial transcriptomics and imaging, we found a central role for lung-resident CD8^{+} T cell–macrophage interactions in impairing alveolar regeneration and driving fibrotic sequelae after acute viral pneumonia. Specifically, IFNγ and TNF derived from CD8^{+} T cells stimulated local macrophages to chronically release IL-1β, resulting in the long-term maintenance of dysplastic epithelial progenitors and lung fibrosis. Notably, therapeutic neutralization of IFNγ + TNF or IL-1β markedly improved alveolar regeneration and pulmonary function. In contrast to other approaches, which require early intervention[10], we highlight therapeutic strategies to rescue fibrotic disease after the resolution of acute disease, addressing a current unmet need in the clinical management of PASC and post-viral disease.

SARS-CoV-2 infection can lead to long-term pulmonary and extrapulmonary symptoms well beyond the resolution of acute disease, a condition collectively termed PASC[1]. The lungs are particularly susceptible to extensive damage during primary infection, potentially resulting in dyspnoea, compromised lung function, radiological abnormalities and pulmonary fibrosis (PASC-PF)[7–9,11–13], which can persist for up to 2 years after infection, in contrast to the majority of extrapulmonary sequelae[14]. Although less appreciated, similar long-term pulmonary deficits have also been described after influenza and SARS-CoV-1 infection, suggesting that this phenomenon may be conserved across different viral aetiologies[2,3]. Despite progress in identifying immune signatures that are dysregulated in respiratory PASC[4,5,8,15–18], little is known regarding their role in driving pathological tissue remodelling, in part owing to the lack of animal models that recapitulate features of post-viral lung disease. Recent research characterizing alveolar regeneration after severe lung injury has identified the accumulation of undifferentiated epithelial progenitors[19–23], the persistence of which has been pathologically associated with chronic diseases such as lung fibrosis[7,9,24]. Currently, the mechanisms that underlie the long-term maintenance of these dysplastic injury-associated cell states after infection and their contributions to post-viral respiratory sequelae remain largely unclear.

[1]Beirne B. Carter Center for Immunology Research, University of Virginia, Charlottesville, VA, USA. [2]Division of Infectious Disease and International Health, Department of Medicine, University of Virginia, Charlottesville, VA, USA. [3]Department of Microbiology, Immunology and Cancer Biology, University of Virginia, Charlottesville, VA, USA. [4]Center for Public Health Genomics, University of Virginia School of Medicine, Charlottesville, VA, USA. [5]Women's Guild Lung Institute, Department of Medicine, Cedars-Sinai Medical Center, Los Angeles, CA, USA. [6]Department of Biomedical Sciences, Cedars-Sinai Medical Center, Los Angeles, CA, USA. [7]Robert and Arlene Kogod Center on Aging, Mayo Clinic, Rochester, MN, USA. [8]Department of Systems Biotechnology, Chung-Ang University, Anseong, Korea. [9]Division of Asthma, Allergy and Immunology, Department of Medicine, University of Virginia, Charlottesville, VA, USA. [10]Division of Pulmonary and Critical Care Medicine, Department of Medicine, University of Virginia, Charlottesville, VA, USA. [11]Department of Biomedical Engineering, University of Virginia, Charlottesville, VA, USA. [12]Department of Microbiology and Immunology, Emory University School of Medicine, Atlanta, GA, USA. [13]Emory Center of Excellence for Influenza Research and Response, Atlanta, GA, USA. [14]School of Medicine, University of Virginia, Charlottesville, VA, USA. [15]Department of Pathology, Cedars-Sinai Medical Center, Los Angeles, CA, USA. [16]These authors contributed equally: Harish Narasimhan, In Su Cheon, Wei Qian, Sheng'en Shawn Hu, Tanyalak Parimon. ✉e-mail: zang@virginia.edu; Peter.Chen@cshs.org; js6re@virginia.edu
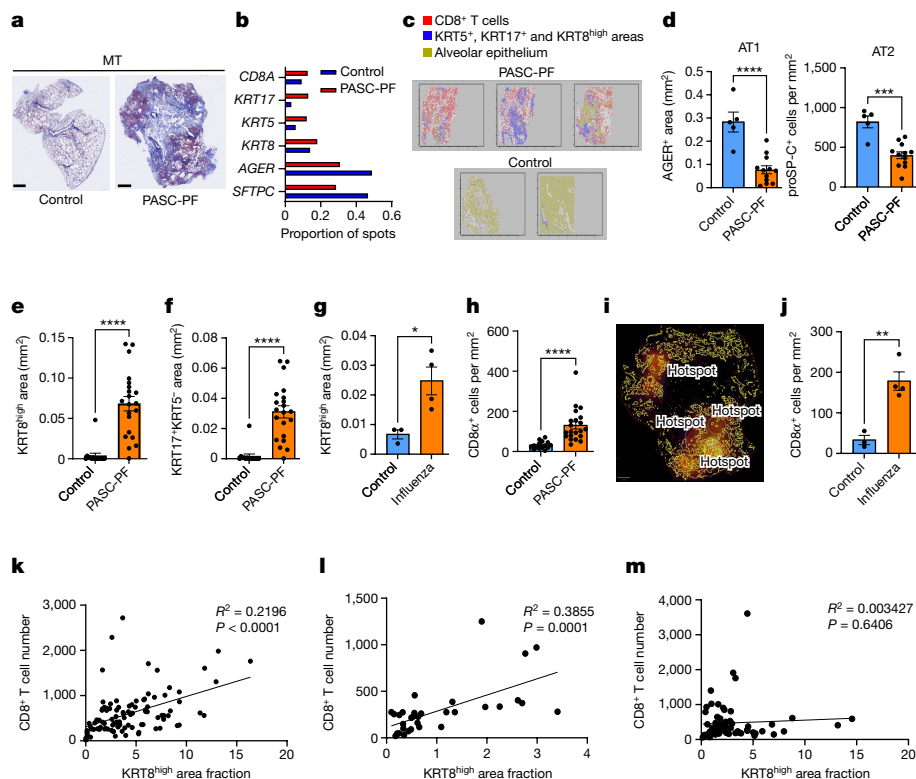
Fig. 1 | An aberrant immune–epithelial progenitor niche is a hallmark of post-viral lung disease. a, Representative Masson's trichrome (MT) images of control and PASC-PF lung sections. Scale bar, 2 mm. **b**, Quantification of the proportion of spots expressing genes characterizing various immune and epithelial populations in control ($n = 2$) and PASC-PF ($n = 3$) lungs. **c**, Visualization of CD8^{+} T cells, areas enriched for KRT5^{+}, KRT8^{high} and KRT17^{+} cells and healthy alveolar epithelium based on gene expression signatures in human control ($n = 2$) and PASC-PF ($n = 3$) lungs. **d**, Quantification of AT1 (AGER[+]) and AT2 (proSP-C[+]) (***$P = 0.0001$) cells in control ($n = 5$) and PASC-PF ($n = 12$) lung sections. **e,f,h**, Quantification of KRT8^{high} transitional (**e**), KRT17^{+}KRT5^{−} aberrant basaloid (**f**) and CD8^{+} T cells (**h**) in control ($n = 15$) and PASC-PF ($n = 21$)

lung sections. **g,j**, Quantification of KRT8^{high} (*$P = 0.0247$) (**g**) and CD8^{+} T cells (**$P = 0.0038$) (**j**) in control ($n = 3$) and influenza-infected ($n = 4$) human lung sections. **i**, Unbiased analysis of the CD8^{+} T cell distribution in a PASC-PF lung section using QuPath. **k–m**, Simple linear regression of the CD8^{+} T cell number and KRT8^{high} area fraction in human PASC-PF lungs (**k**; 5–7 random fields per lung, $n = 21$ lungs), human lungs after influenza infection (**l**; 8 random fields per lung, $n = 4$ lungs) and IPF lung sections (**m**; 5–7 random fields per lung, $n = 13$ lungs). Statistical analysis was performed using two-tailed unpaired t-tests (**d**, **e–h** and **j**); *$P < 0.05$, **$P < 0.01$, ***$P < 0.001$, ****$P < 0.0001$; NS, not significant. Data are mean ± s.e.m.

Aberrant immune–epithelial progenitor niche

We examined diseased lungs from two cohorts of patients with PASC-PF who underwent lung transplantation at Cedars-Sinai Medical Center and University of Virginia (Supplementary Tables 1 and 2). None of the patients had any pre-existing lung disease before infection that necessitated a lung transplant. SARS-CoV-2 was absent by PCR of nasal swabs during routine clinical testing as part of the pre-transplant evaluation and was also not evident in the explanted lungs (Extended Data Fig. 1a). Lung histology showed extensive immune cell infiltration and collagen deposition in the alveolar epithelium (Fig. 1a and Extended Data Fig. 1b). Given the heterogenous distribution of tissue pathology, we performed spatial transcriptomics analysis of PASC-PF and control lungs to evaluate potentially distinct microenvironments within healthy and diseased lung areas (Extended Data Fig. 1c,d). Using an agnostic evaluation by gene set enrichment analysis, we observed robust upregulation of pathways associated with extracellular matrix deposition and fibrosis, as well as inflammation, within PASC-PF lungs compared with control lungs (Extended Data Fig. 1e). Expression of genes associated with alveolar epithelial type 1 and 2 (AT1 and AT2) cells was reduced, whereas that of genes characterizing dysplastic epithelial progenitors[19–23,25,26] was elevated in PASC-PF lungs (Fig. 1b and Extended Data Fig. 1f). Consistent with active inflammatory processes, CD8^{+} T cell gene expression was enriched in PASC-PF lungs (Fig. 1b and Extended Data Fig. 1f). Furthermore, we found that large areas of PASC-PF lungs were

populated by CD8^{+} T cells, dysplastic epithelial progenitors and CD4^{+} T cells (Fig. 1c and Extended Data Fig. 1f,g), whereas control lungs were primarily composed of alveolar epithelial cells (Fig. 1c and Extended Data Fig. 1f). Notably, the sporadic pockets of alveolar epithelium-rich areas in PASC-PF lungs were geographically distinct from CD8^{+} T cells and dysplastic repair markers (Fig. 1c). Consistent with this, a mild correlation was observed between the distribution of CD8^{+} T cells and dysplastic epithelial progenitors (Extended Data Fig. 1h).

To validate these findings, we used multicolour immunofluorescence analysis in a larger cohort of samples and found reduced levels of AT1 and AT2 cells in PASC-PF lungs compared with in the control lungs[27] (Fig. 1d and Extended Data Fig. 1i). Chronic persistence of ectopic KRT5^{+} pods, KRT8^{high} transitional cells and KRT5^{−} KRT17^{+} aberrant basaloid cells was observed in PASC-PF lungs, in proximity to areas exhibiting myofibroblast activity[7,9,12] (Fig. 1e,f and Extended Data Fig. 1j–n). Thus, PASC-PF histologically resembles other fibrotic diseases such as idiopathic pulmonary fibrosis (IPF), including the sustained loss of functional alveolar epithelial cells and the persistence of metaplastic KRT5^{+} pods, KRT8^{high} transitional cells and KRT17^{+}KRT5^{−} aberrant basaloid cells[25,26,28,29] (Extended Data Fig. 1n). Notably, these features were also observed in human lungs with fibrotic remodelling after influenza viral infection (Fig. 1g and Extended Data Fig. 1q–t).

Previously, we reported that CD8^{+} T cell abundance in the bronchoalveolar lavage (BAL) fluid was associated with impaired lung function in convalescent individuals recovering from COVID-19[4,5]. Similarly,

CD8^{+} T cell numbers were elevated in PASC-PF lungs (Fig. 1h) as well as in IPF lungs compared with in the control lungs (Extended Data Fig. 1o,p). The mild correlation in localization revealed by spatial transcriptomics was corroborated by a marked spatial association between CD8^{+} T cells, and areas of dysplastic repair in PASC-PF lungs (Fig. 1i,k and Extended Data Fig. 2a–f). Notably, this phenomenon was conserved in lungs with fibrosis associated with influenza viral infection, which exhibited extensive CD8^{+} T cell infiltration (Fig. 1j and Supplementary Table 3) as well as evidence of aberrant immune–epithelial progenitor niches (Fig. 1l and Extended Data Fig. 2g). Similar niches were also observed in the lungs from two organ donors with a previous history of influenza viral infection (evidenced by high frequency of M58-66 epitope-specific CD8^{+} T cells) (Extended Data Fig. 2h,i). Notably, this correlation between CD8^{+} T cells and dysplastic epithelial progenitors was not seen in lungs from healthy donors or individuals with IPF (Fig. 1m and Extended Data Fig. 2j–n). Collectively, these data indicate that the spatiotemporal colocalization of CD8^{+} T cells and areas of dysplastic repair is a unique feature of post-viral pulmonary fibrosis and supports a role for immune–epithelial progenitor interactions in chronic lung sequelae.

A mouse model of post-viral lung sequelae

To investigate the role of immune–epithelial progenitor interactions, we aimed to develop a mouse model to capture the cellular and pathological features observed in PASC-PF lungs. We used a mouse-adapted (MA-10) strain of the SARS-CoV-2 virus to productively infect wild-type mice[30]. As ageing is associated with an increased propensity to develop lung fibrosis after alveolar injury, we included both young and aged mice in our study[31,32]. Aged C57BL/6 mice infected with SARS-CoV-2 MA-10 exhibited increased morbidity and mortality compared with young mice (Extended Data Fig. 3a). Yet, despite the marked acute inflammation and tissue damage (at 10 days post-infection (d.p.i.))[30,33] (Extended Data Fig. 3b), only moderate pathology restricted to the subpleural regions was observed during the chronic phase (35 d.p.i.) of infection (Fig. 2a and Extended Data Fig. 3c). Moreover, KRT8^{high} transitional cell abundance remained unchanged between aged naive and infected (35 d.p.i.) mouse lungs (Fig. 2b and Extended Data Fig. 3d,e). We next tested SARS-CoV-2 MA-10 infection in aged BALB/c mice, which was previously reported to induce more robust inflammation and fibrotic sequelae than in C57BL/6 mice[31] (Extended Data Fig. 3f,g). Persistent immune cell infiltration was observed within peribronchiolar regions at 35 d.p.i., but minimal signs of collagen deposition were noted within the alveolar epithelium (Fig. 2c and Extended Data Fig. 3h). Consistent with previous observations[31], BALB/c mice did not maintain pulmonary CD8^{+} T cells and KRT8^{high} transitional cells (Fig. 2d and Extended Data Fig. 3i,j)—a prominent feature of human PASC-PF (Fig. 1e,h), despite the substantial alveolar damage during acute disease (Extended Data Fig. 3g). Finally, we infected transgenic mice expressing the human ACE2 receptor under the cytokeratin 18 promoter (K18-hACE2) with the wild-type SARS-CoV-2 virus (USA-WA1/2020), which is known to result in perivascular and alveolar inflammation[34] (Extended Data Fig. 3k). However, alveolar injury was minimal at chronic timepoints (Fig. 2e and Extended Data Fig. 3l), with no appreciable differences in CD8^{+} T or KRT8^{high} transitional cells between infected and naive mice (Fig. 2f and Extended Data Fig. 3m,n). Thus, SARS-CoV-2 infection in these three mouse models did not recapitulate key features of tissue pathology and dysplastic lung repair observed in human PASC-PF.

Previously, we reported persistent lung inflammation and tissue pathology after influenza virus infection, particularly in aged C57BL/6 mice[4,32,35]. We therefore infected young and aged wild-type C57BL/6 mice with influenza H1N1 A/PR8/34 strain (IAV), which causes substantial viral pneumonia and alveolar damage[32,35]. Aged mice exhibited increased morbidity and mortality after IAV infection compared with the young mice (Extended Data Fig. 3o). In contrast to SARS-CoV-2

infection, we observed persistent immune cell infiltration and collagen deposition in the alveolar epithelium, particularly in aged mice, up to 60 d.p.i. (Fig. 2g and Extended Data Fig. 3p). Although both young[19] and aged IAV-infected mice had dysplastic repair areas, aged lungs maintained significantly larger KRT5^{+} and KRT8^{high} areas as well as higher levels of CD8^{+} T cells, similar to human PASC-PF lungs (Fig. 2h,i and Extended Data Figs. 3q and 4a,b). In addition to the quantitative differences, aged KRT8^{high} transitional cells also expressed higher levels of PDLIM7—a marker that was recently shown to capture mouse transitional cells bearing high transcriptional similarity with aberrant basaloid cells in human patients with IPF[36] (Extended Data Fig. 4c,d). Such qualitative changes were also observed in an independent dataset of post-bleomycin injury, suggesting intrinsic age-associated differences in regenerative cell states[37] (Extended Data Fig. 4e). Notably, lungs exhibited considerable inflammation and collagen deposition, with high levels of CD8^{+} T cells and dysplastic epithelial progenitors, up to 8 months after infection (Extended Data Fig. 4f–m).

SARS-CoV-2 infection in both aged C57BL/6 and BALB/c mice induced loss of AT2 cells, whereas the AT1 cell compartment was relatively unaffected throughout the course of disease (Extended Data Fig. 5a–e). This finding contrasts with human COVID-19, in which extensive infection and loss of AT1 cells has been previously reported[38,39] (Fig. 1d). However, IAV infection of both young and aged C57BL/6 mice triggered a substantial decrease in AT2 and AT1 cells during acute disease (Extended Data Fig. 5f–i), as seen in the lungs of individuals with influenza at autopsy (Extended Data Fig. 1s). Recent work demonstrating the necessity of AT1 cell loss in tissue remodelling and the emergence of the KRT8^{high} transitional cell state[40] may explain the persistence of dysplastic epithelial progenitors in IAV-infected mice but not in mice infected with SARS-CoV-2 MA-10. The differential AT1 cell death observed during acute infection across the models (Fig. 2j) is probably a reflection of the distinct tropism of the viruses in mice[30,41] (Extended Data Fig. 5j).

Although dysplastic repair areas were observed in both young[19,22] and aged IAV-infected mice, only aged lungs did not fully regenerate the alveolar epithelium by 30 d.p.i. (Extended Data Fig. 5h,i). The observed cellular changes were associated with sustained defects in pulmonary function in aged mice up to 60 d.p.i. after IAV pneumonia, mimicking the persistent impairment in lung function observed in patients with respiratory PASC[4,12] (Extended Data Fig. 5k,l). Thus, after extensive evaluation of various mouse viral pneumonia models, IAV infection in aged mice was found to exhibit close histopathological alignment with features of post-viral disease observed in human PASC-PF and influenza-fibrosis lungs, supporting its use in studying the mechanisms underlying viral-infection-mediated lung fibrosis.

Exuberant CD8^{+} T cell activity impairs recovery

Similar to human PASC-PF lungs, we observed a spatial association between CD8^{+} T cells and dysplastic repair areas in aged IAV-infected mice, suggesting that aberrant immune–epithelial progenitor niches are conserved across different species during post-viral lung sequelae (Fig. 2k,l and Extended Data Fig. 6a–c). To understand the role of CD8^{+} T cells, we treated aged IAV-infected mice with CD8^{+} T cell depleting antibody (anti-CD8) or control antibody (IgG) starting from 21 d.p.i. (Fig. 2m). This post-acute timepoint was chosen to ensure that there was no interference with the essential antiviral activities of CD8^{+} T cells during infection[32] (Extended Data Fig. 6d). CD8^{+} T cell depletion improved the histological features of disease (Extended Data Fig. 6e–g) and, importantly, reduced KRT5^{+} and KRT8^{high} areas (Fig. 2n,o and Extended Data Fig. 6h). Moreover, CD8^{+} T cell depletion markedly increased AT1 and AT2 cells (Fig. 2p and Extended Data Fig. 6i) and improved lung function (Fig. 2r), suggesting that exuberant CD8^{+} T cell activity in the post-viral lung impaired alveolar regeneration, inducing chronic deficits in gas-exchange function.
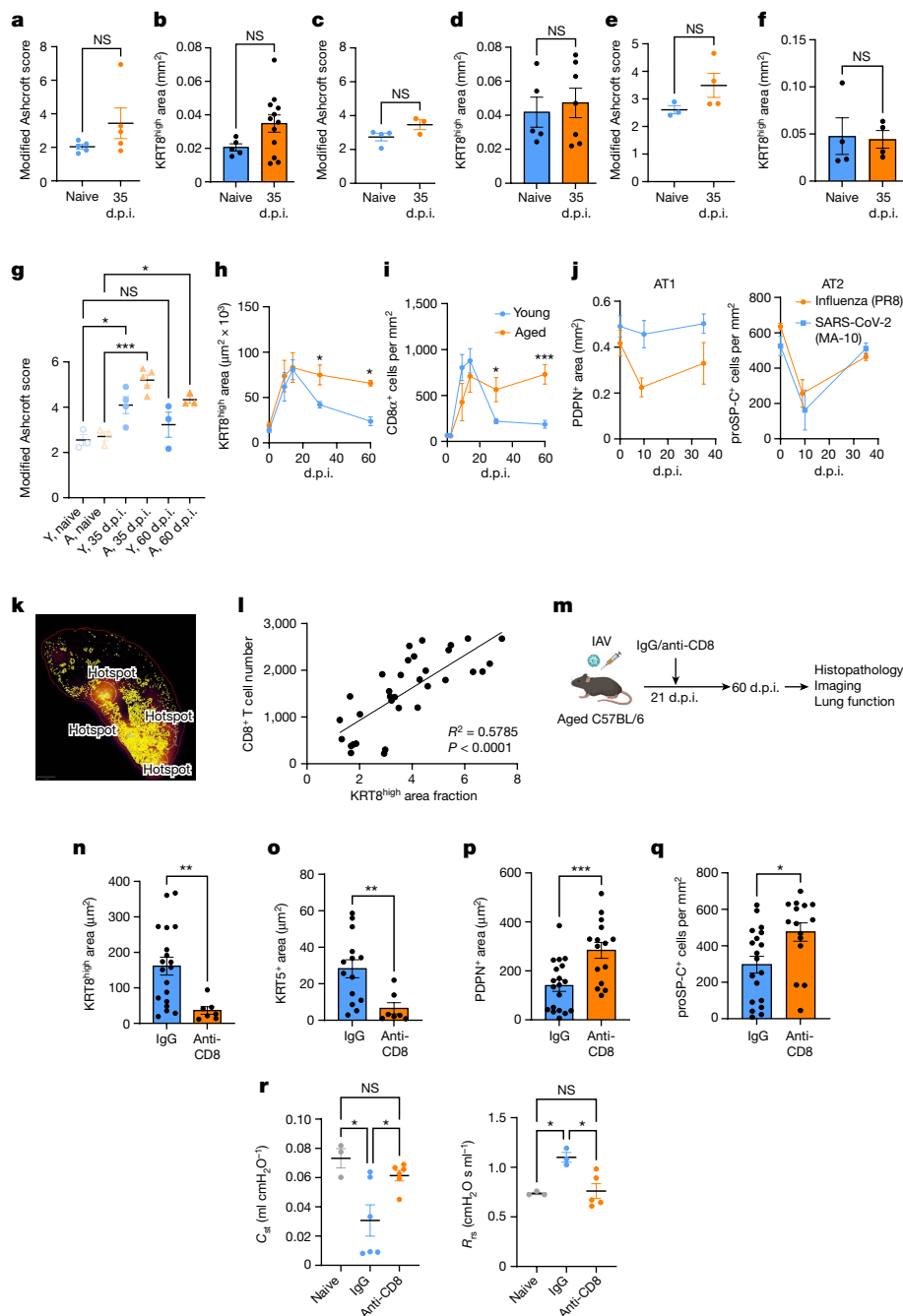
Fig. 2 | Persistent CD8⁺ T cell activity impairs alveolar regeneration in a mouse model of post-viral fibrosis. a,**b**, Evaluation of fibrotic disease (**a**; $n = 5$ (naive) and $n = 5$ (MA-10)) and KRT8^{high} area (**b**; $n = 5$ (naive) and 12 (MA-10)) in aged C57BL/6 mice at 35 d.p.i. after infection with MA-10. **c**,**d**, Evaluation of fibrotic disease (**c**; $n = 4$ (naive) and $n = 3$ (MA-10)) and KRT8^{high} area (**d**; $n = 5$ (naive) and $n = 7$ (MA-10)) in aged BALB/c mice at 35 d.p.i. after infection with MA-10. **e**,**f**, Evaluation of fibrotic disease (**e**; $n = 3$ (naive) and $n = 4$ (WA-1)) and KRT8^{high} area (**f**; $n = 4$ (naive), $n = 4$ (WA-1)) in aged K18-hACE2 mice at 35 d.p.i. after infection with WA-1. **g**, Evaluation of fibrotic disease in young (Y) and aged (A) C57BL/6 mice after infection with influenza H1N1 A/PR8/34. $n = 3$–5 per timepoint. *$P = 0.0378$ (left) and 0.0412 (right), ***$P = 0.0004$. **h**,**i**, KRT8^{high} transitional (**h**; *$P = 0.0112$ (left) and 0.0251 (right)) and CD8⁺ T cells (**i**; *$P = 0.0190$ (left), ***$P = 0.0006$ (right)) in young and aged lungs after IAV infection. $n = 4$–11 per timepoint. **j**, Quantification of AT1 (PDPN⁺) and AT2 (proSP-C⁺) cells after SARS-CoV-2 MA-10 and IAV infection in aged C57BL/6 mice. $n = 3$–4 per

timepoint. **k**, Unbiased analysis of the CD8⁺ T cell distribution in an aged IAV-infected lung at 60 d.p.i. by QuPath. **l**, Linear regression of CD8⁺ T cells and KRT8^{high} area in aged IAV-infected lungs at 60 d.p.i. 5–7 random fields per lung; $n = 4$. **m**, The experimental design for CD8⁺ T cell depletion. The diagram was created using BioRender. **n–r**, Quantification of KRT8^{high} (**n**; **$P = 0.0069$) and KRT5⁺ (**o**; **$P = 0.0085$) area ($n = 14$–19 (control IgG), $n = 7$ (anti-CD8)); AT1 (PDPN⁺) area (**p**; ***$P = 0.0009$) and AT2 (proSP-C⁺) cells per mm² (**q**; $P = 0.0136$) ($n = 19$ (control IgG) and $n = 15$ (anti-CD8)); and evaluation of lung function (**r**; compliance (C_{st}); *$P = 0.0172$ (left) and 0.0338 (right); resistance of the respiratory system (R_{rs}); *$P = 0.0183$ (left) and 0.0147 (right)) in aged IAV-infected mice (60 d.p.i.) treated with anti-CD8 or IgG antibody ($n = 3$–6 per timepoint). Data are representative of two (**a**–**l**) or three (**m**–**r**) independent experiments. Statistical analysis was performed using two-tailed unpaired t-tests (**a**–**f** and **n**–**q**), ordinary one-way analysis of variance (ANOVA) (**g** and **r**) and two-way ANOVA (**h** and **i**). Data are mean ± s.e.m.
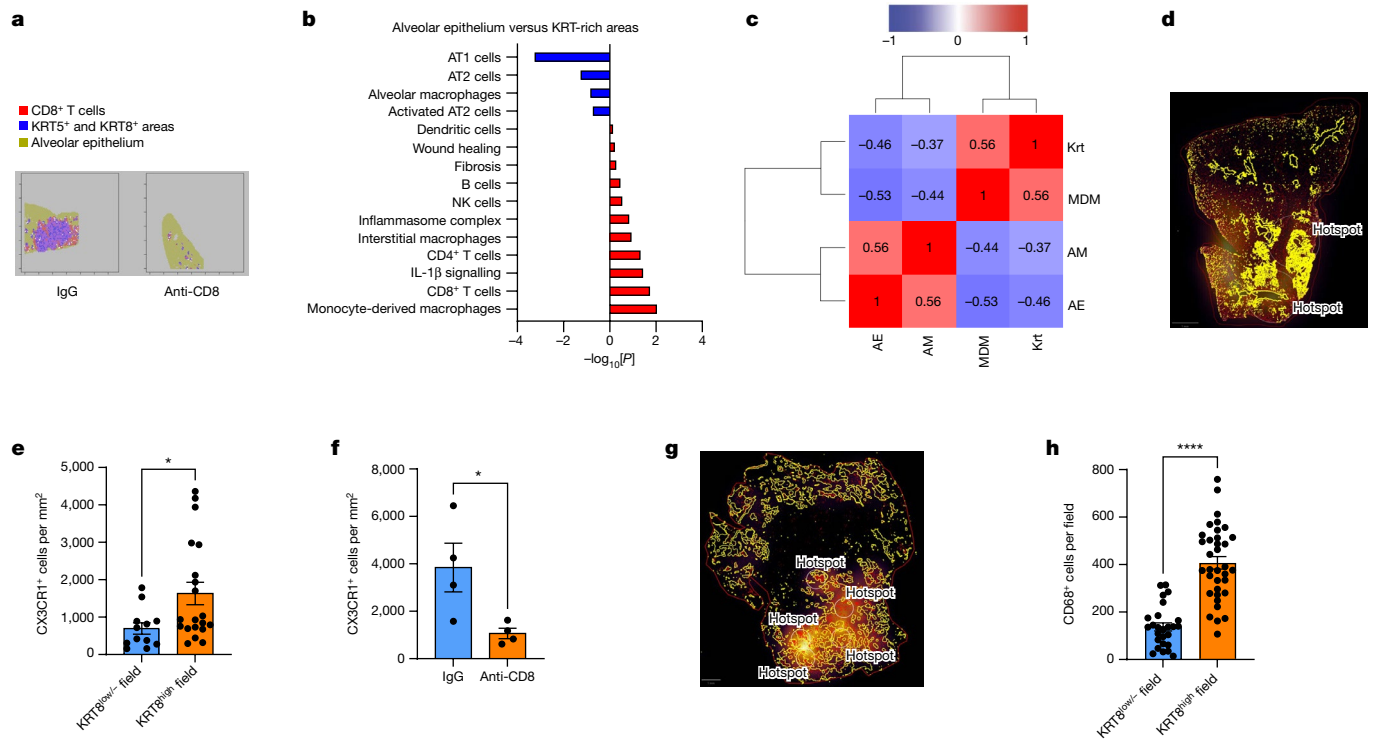
Fig. 3 | Spatial transcriptomics reveals a CD8⁺ T cell–macrophage–epithelial progenitor niche that drives dysplastic lung repair. a,b, Visualization (**a**) and quantification (**b**) of various immune and epithelial cell subsets as well as signalling pathways in areas enriched for KRT5⁺ and KRT8^high cells and healthy alveolar epithelium. **c,** The physical distribution of monocyte-derived macrophages (MDM), alveolar macrophages (AM), KRT5⁺ and KRT8^high areas (Krt) and healthy alveolar epithelium (AE) in aged IAV-infected (60 d.p.i.) mouse lungs. **d,** Unbiased analysis of the CX3CR1⁺ macrophage distribution in aged IAV-infected (60 d.p.i.) lungs. **e,** Quantification of the CX3CR1⁺ macrophage distribution within KRT8^(−/low) (healthy) and KRT8^high (diseased) fields in aged IAV-infected (60 d.p.i.) lungs. 3–5 random fields per lung; *n* = 4. *P = 0.0429. **f,** Quantification of CX3CR1⁺ macrophages in aged IAV-infected (60 d.p.i.) lungs that were treated with control IgG antibody or anti-CD8. *n* = 4. *P = 0.0380. **g,** Unbiased analysis of the distribution of CD68⁺ macrophages in a human PASC-PF lung using QuPath. **h,** Quantification of CD68⁺ macrophages within KRT8^(−/low) (healthy) and KRT8^high (diseased) fields in human PASC-PF lungs. 5–7 random fields per lung; *n* = 5. Statistical analysis was performed using two-tailed unpaired *t*-tests (**e**, **f** and **h**). Data are mean ± s.e.m.

Notably, depletion of CD8⁺ T cells resolved KRT5⁺ but not KRT8^high areas in young mice and also did not substantially affect lung pathology (Extended Data Fig. 6j–m). To further examine whether this effect is due to intrinsic changes within the CD8⁺ T cell compartment with age, we transferred lung CD8⁺ T cells from young or aged mice after IAV infection (21 d.p.i.) into infection-matched congenic young recipients. Three weeks after transfer, AT2 cell numbers were reduced after transfer of CD8⁺ T cells from aged lungs compared with young lungs, while no significant differences were observed in KRT8^high areas or AT1 levels (Extended Data Fig. 6n–q). These data suggest that aged CD8⁺ T cell transfer alone is not sufficient to cause the marked phenotype observed in virus-infected aged mice, implicating the aged microenvironment as a key mediator of chronic lung pathology. To dissect their respective contributions in impairing lung recovery, we also used low-dose and high-dose anti-CD8 treatment to deplete circulating and pulmonary CD8⁺ T cells, respectively[32]. We found that the therapeutic effects were dependent on eliminating pulmonary CD8⁺ T cells but not circulating CD8⁺ T cells[32] (Extended Data Fig. 6r), suggesting that lung-resident CD8⁺ T cells are required for the long-term maintenance of dysplastic epithelial progenitors. Together, our results strongly implicate the activity of CD8⁺ T cells persisting in the lungs after viral pneumonia in driving chronic pulmonary sequelae.

Spatial profiling reveals immune–epithelial interactions

We performed spatial transcriptomics analysis of aged IAV-infected mouse lungs (60 d.p.i.) treated with IgG or anti-CD8 (Extended Data Fig. 7a–c). In addition to the histopathological similarities, dysplastic repair areas of aged IAV-infected mouse lungs were enriched with the genes and pathways that were differentially upregulated within pathological areas of human PASC-PF lungs (Extended Data Fig. 7d–f). This transcriptional congruence was dependent on CD8⁺ T cell activity, as anti-CD8-treated mice exhibited reduced conservation of human PASC-PF-specific genes and signalling pathways compared with the controls (Extended Data Fig. 7g–i).

Moreover, a strong spatial association was observed between the gene expression signatures of CD8⁺ T cells, and KRT5⁺ and KRT8^high areas of dysplastic repair, similar to human PASC-PF lungs (Fig. 3a). Signatures of KRT5⁺ and KRT8^high progenitors were substantially reduced in anti-CD8-treated lungs, with a concomitant increase in healthy alveolar epithelial cells (Fig. 3b and Extended Data Fig. 7l,m). Several pathways associated with inflammatory responses were highly active within areas of dysplastic repair, whereas processes associated with growth factor activity and vascular regeneration were prominently observed in the healthy alveolar epithelium (Extended Data Fig. 7j). Previously reported transcriptional signatures of KRT8^high transitional cells[20–22] and human aberrant basaloid cells[25,26] were strongly enriched within areas of dysplastic repair (Extended Data Fig. 7k). Furthermore, monocyte-derived macrophages, CD4⁺ T cells, interstitial macrophages, B cells and natural killer cells were enriched in dysplastic repair areas, while pro-repair tissue-resident alveolar macrophages, AT1 and AT2 cells were primarily observed within the healthy alveolar epithelium (Fig. 3b and Extended Data Fig. 7l–p). After conducting a correlation analysis, we found that CD8⁺ T cells and monocyte-derived macrophages physically clustered around KRT5⁺

Article

and KRT8^{high} areas of dysplastic repair and were excluded from areas enriched with alveolar macrophages and mature alveolar epithelial cells (Fig. 3c and Extended Data Fig. 7l–p). The physical distribution of these niches corresponded with the expression pattern of a gene set indicative of fibrosis, particularly enriched within KRT5^{+} and KRT8^{high} areas, and was reduced in anti-CD8-treated lungs (Extended Data Fig. 7q).

Immunostaining identified a similar enrichment of CX3CR1^{+} monocyte-derived macrophages within areas of dysplastic repair (Fig. 3d,e and Extended Data Fig. 8a). Notably, CD8^{+} T cell depletion resulted in decreased CCL2 levels and CX3CR1^{+} macrophages, suggesting a potential role in macrophage recruitment and maintenance in post-viral lungs[36] (Fig. 3f and Extended Data Fig. 8b–d). A similar increase in the gene signature of monocyte-derived macrophages was observed within PASC-PF lungs (Extended Data Fig. 8e), and was particularly enriched within dysplastic repair areas (Extended Data Fig. 8f–h), and corroborated by immunostaining (Fig. 3g,h and Extended Data Fig. 8i–k). Together, our data revealed a conserved finding in both mouse and human post-viral lungs, where CD8^{+} T cells are present in fibrotic regions, in proximity to fibroproliferative mediators such as monocyte-derived macrophages and dysplastic epithelial progenitors, constituting an aberrant niche after acute respiratory viral infections.

CD8^{+} T cell–macrophage axis

We postulated that the interactions between CD8^{+} T cells, macrophages and epithelial progenitors within this aberrant niche generated molecular cues to create a profibrotic microenvironment. IL-1R signalling and inflammasome activity were enriched in dysplastic repair areas compared with in the healthy alveolar epithelium in human PASC-PF (Fig. 4a and Extended Data Fig. 9a), and this was conserved with aged IAV-infected mouse lungs (Fig. 4b and Extended Data Fig. 9b). Notably, IL-1β has been shown to promote the expansion and persistence of transitional KRT8^{high} cells after alveolar injury[22,42]. We found that CD64^{+} macrophages were major producers of proIL-1β in IAV-infected aged lungs (Fig. 4c and Extended Data Fig. 9c). As mature IL-1β release from cells requires caspase-1-mediated proteolytic cleavage[43], we examined caspase-1 activity and observed a substantial reduction within lung macrophages after anti-CD8 treatment (Fig. 4d and Extended Data Fig. 9d,e), while inflammasome gene signatures were also attenuated (Extended Data Fig. 9f), therefore implicating CD8^{+} T cells in chronic inflammasome activation and IL-1β release by macrophages.

PASC-PF lungs were found to contain high levels of IFNγ^{+}CD8^{+} and TNF^{+}CD8^{+} T cells, similar to aged IAV-infected lungs[44,45] (Fig. 4e,f and Extended Data Fig. 9g–i). Moreover, areas of dysplastic repair were enriched with IFNγ and TNF signalling in human PASC-PF lungs (Extended Data Fig. 9j). We therefore investigated whether IFNγ and TNF mediate inflammasome activation; we treated aged IAV-infected mice with neutralizing antibodies against both IFNγ and TNF and observed decreased caspase-1 activity (Fig. 4g). As this effect phenocopies anti-CD8 treatment (Fig. 4d), we directly tested whether CD8^{+} T cell-derived IFNγ and TNF regulated macrophage activity ex vivo (Fig. 4h) and observed that CD8^{+} T cells indeed augmented macrophage Il1b mRNA expression (Extended Data Fig. 9k), caspase-1 activity (Fig. 4i) and IL-1β release (Fig. 4j). The synergistic activity between macrophages and CD8^{+} T cells to produce IL-1β was lost when the cells were isolated from naive mice, suggesting that previous infection is necessary to prime the cells (Extended Data Fig. 9l). Although IL-1β release was significantly reduced after treatment with either IFNγ or TNF neutralizing antibody, neutralization of both cytokines was most effective, pointing to an additive effect in stimulating macrophages (Fig. 4k). Similarly, we observed decreased IL-1β levels in the BAL fluid after anti-CD8 (Fig. 4l) or anti-IFNγ + anti-TNF treatment (Fig. 4m).

We next examined whether macrophage-derived IL-1β is a negative regulator of AT2-to-AT1 transdifferentiation using a 2D primary AT2 cell culture model known to induce spontaneous differentiation into AT1 cells through the KRT8^{high} transitional cell state[46,47] (Fig. 4n). AT1 cell marker expression was reduced after exposure to conditioned medium from CD8^{+} T cell–macrophage coculture compared with macrophages alone, and was rescued after IL-1β neutralization (Extended Data Fig. 9m). By contrast, transitional cell marker expression exhibited the opposite pattern, with increased levels in the coculture group and a substantial reduction after anti-IL-1β treatment[22] (Fig. 4o). Collectively, our results suggest that exuberant CD8^{+} T cell–macrophage interactions promote chronic IL-1β release to inhibit AT2 transdifferentiation by arresting the cells in the KRT8^{high} transitional state.

Therapeutic enhancement of alveolar regeneration

Our data thus far indicate a pathological role for CD8^{+} T cells persisting in post-viral lungs in the development of chronic pulmonary sequelae. As depletion of CD8^{+} T cells is not a clinically feasible treatment strategy, we examined the therapeutic efficacy of neutralizing the cytokines that act as effectors of the profibrotic CD8^{+} T cell. Blocking IFNγ and TNF activity in aged IAV-infected mice ameliorated fibrotic sequelae compared with untreated controls (Fig. 5a and Extended Data Fig. 10a,b). Moreover, IFNγ and TNF neutralization diminished KRT5^{+} and KRT8^{high} areas of dysplastic repair (Fig. 5b,c and Extended Data Fig. 10c) and enhanced alveolar regeneration as evidenced by the increased numbers of AT1 and AT2 cells (Fig. 5d,e and Extended Data Fig. 10c). The observed cellular changes after treatment also conferred physiological benefit by restoring pulmonary function (Fig. 5f and Extended Data Fig. 10d).

Next, we tested the efficacy of neutralizing IL-1β in IAV-infected aged mice and observed substantial attenuation of lung fibrosis and improved alveolar regeneration, phenocopying outcomes after CD8^{+} T cell depletion and neutralization of IFNγ and TNF (Fig. 5g–k and Extended Data Fig. 10e–h). Further supporting the therapeutic use of IL-1β blockade after infection, we found improved lung function in anti-IL-β-treated mice (Fig. 5l and Extended Data Fig. 10i). Notably, improvement in outcomes after IL-1β neutralization were seen only in aged mice but not young mice, which is probably due to the sustained elevation of IL-1β observed exclusively in aged mice (Extended Data Fig. 10j,k). Consistent with these data and a recent study identifying increased BAL IL-1β levels in respiratory PASC[8], we found that circulating IL-1β levels were elevated in convalescent individuals recovering from COVID-19 exhibiting persistent pulmonary function deficits (Fig. 5m and Supplementary Table 4), implicating chronic IL-1β activity in the failure to restore normal lung function.

Given the efficacy of IL-6 neutralization in treating acute COVID-19[48] and preclinical data suggesting rescue of fibrotic disease after bleomycin injury[49], we also examined the efficacy of IL-6 blockade in our model (Extended Data Fig. 10l). In contrast to the neutralization of IFNγ + TNF or IL-1β, blocking IL-6 activity in post-viral lungs did not improve fibrotic sequelae, KRT8^{high} and KRT5^{+} areas, alveolar regeneration or pulmonary function (Extended Data Fig. 10m–r). Although KRT5^{+} progenitors were previously shown to migrate to the distal airspace in response to IL-6 signalling[49], our data indicate that their maintenance on pod formation after infection is independent of IL-6 signalling.

Collectively, these data support the neutralization of IFNγ + TNF or IL-1β in the post-acute stage of viral infection as viable therapeutic options to augment alveolar regeneration and dampen fibrotic sequelae observed after respiratory viral infections (Extended Data Fig. 10s).

Discussion

Immune-derived cues have recently been shown to influence lung repair[3,22,35,42,50]; however, their role in post-viral fibrosis remains unexplored. Here we describe a spatially defined aberrant immune–
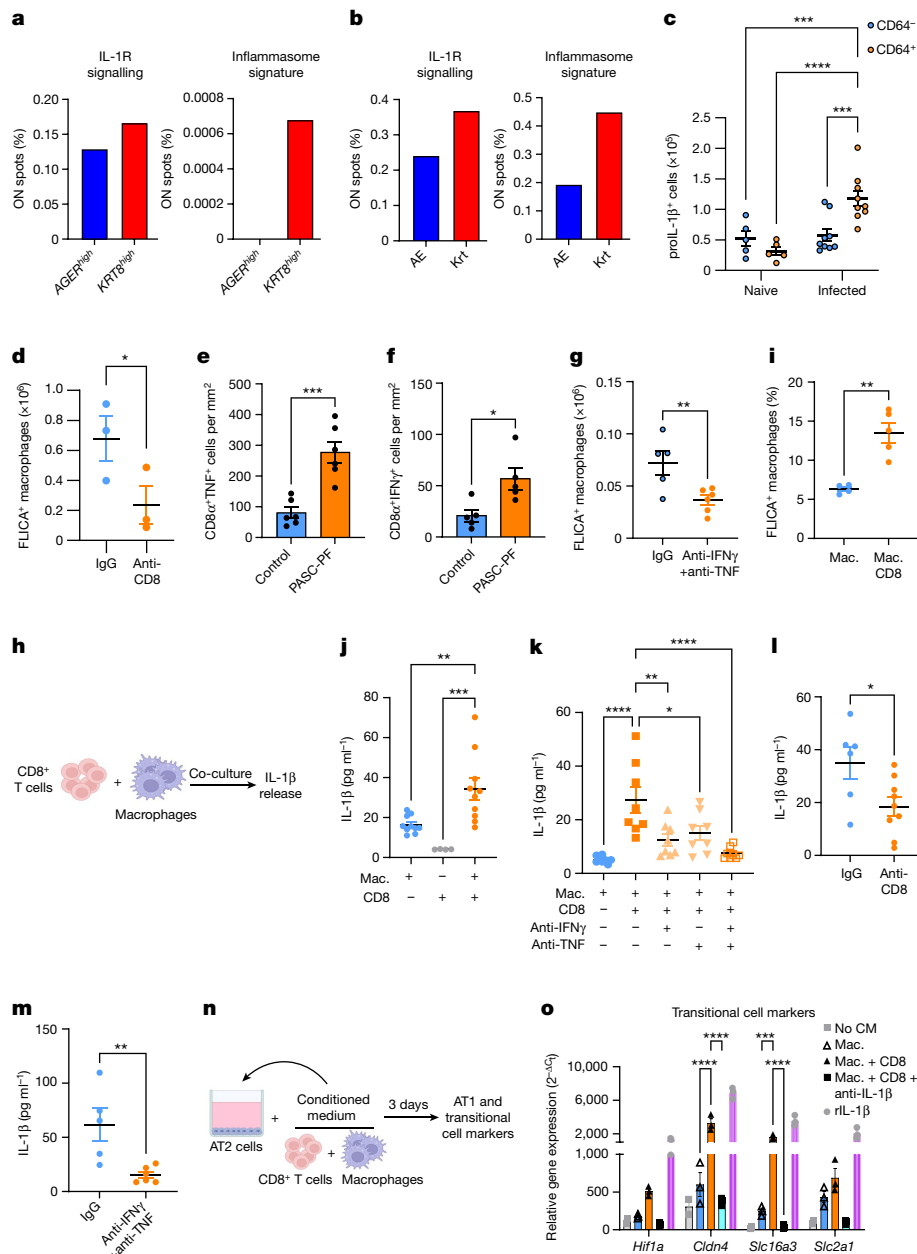
Fig. 4 | CD8+ T cells promote macrophage-mediated IL-1β release through IFNγ and TNF. a,b, Gene expression signatures passing the cutoff (ON spots, %) for IL-1R signalling and inflammasome activity in *AGER^high* (healthy) and *KRT8^high* (diseased) areas within human PASC-PF lungs (**a**; *n* = 3) and AE (alveolar epithelium-rich; healthy) and Krt (*KRT8^high* and *KRT5*+-rich; diseased) in aged IAV-infected (60 d.p.i.) mouse lungs (**b**; *n* = 2). **c,** Flow cytometry quantification of proIL-1β+ cells in aged naive (*n* = 5) and IAV-infected (42 d.p.i.; *n* = 9) mice. ****P* = 0.0009 (left) and 0.0004 (right). **d,** Caspase-1 activity (FLICA) in aged IAV-infected (42 d.p.i.) lungs after control IgG antibody (*n* = 3) or anti-CD8 (*n* = 3) treatment. **P* = 0.0431. **e,f,** Quantification of TNF+ (**e**; ****P* = 0.0005) and IFNγ+ (**f**; **P* = 0.0179) CD8+ T cells in human control and PASC-PF lungs. *n* = 5–6 per group. **g,** Caspase-1 activity in the lungs of aged IAV-infected (42 d.p.i.) after control IgG antibody (*n* = 5) or anti-IFNγ + anti-TNF (*n* = 6) treatment. ***P* = 0.0063. **h,** Schematic of the ex vivo macrophage (mac.) and CD8+ T cell coculture system. **i,** Caspase-1 activity. *n* = 4–5 wells per condition pooled from

2 mice. ***P* = 0.0017. **j,k,** Evaluation of IL-1β release by ELISA without (**j**; *n* = 4–10 wells per condition pooled from 4 mice; ***P* = 0.0075, ****P* = 0.0008) or with (**k**; *n* = 8 wells per condition pooled from 5 mice; **P* = 0.0206, ***P* = 0.0030) in vitro antibody blockade in the coculture. **l,m,** Evaluation of IL-1β levels in the BAL fluid of aged IAV-infected mice (42 d.p.i.) after IgG antibody (*n* = 6) or anti-CD8 (*n* = 9) treatment (**P* = 0.0265) (**l**), or IgG antibody (*n* = 5) or anti-IFNγ + anti-TNF neutralizing antibody (*n* = 6) treatment (**m**; ***P* = 0.0090). **n,** The experimental design for the 2D AT2 culture system. **o,** Transitional cell marker gene expression after exposure to conditioned medium (CM). *n* = 2–3 wells per condition pooled from 4 mice. ****P* = 0.0007. Data are representative of two (**c–g**, **i** and **o**) or three (**j**, **k** and **m**) independent experiments. Statistical analyses were performed using two-tailed unpaired *t*-tests (**d–g** and **i,l,m**), ordinary one-way ANOVA (**j**, **k**), and two-way ANOVA (**c,o**). Data are mean ± s.e.m. The diagrams in **h** and **n** were created using BioRender.

epithelial progenitor niche—a unique feature of lungs after viral fibrosis, but not after IPF. With insights from patient samples, we established a mouse model of post-viral lung fibrosis to demonstrate a causal role for exuberant interactions between CD8+ T cells, macrophages and

epithelial progenitors in driving chronic sequelae and fibrosis after viral pneumonia. Whether the prolonged maintenance and activity of lung CD8+ T cells is a result of excessive TGF-β signalling[9], chronic persistence of viral remnants[51,52] or other independent mechanisms
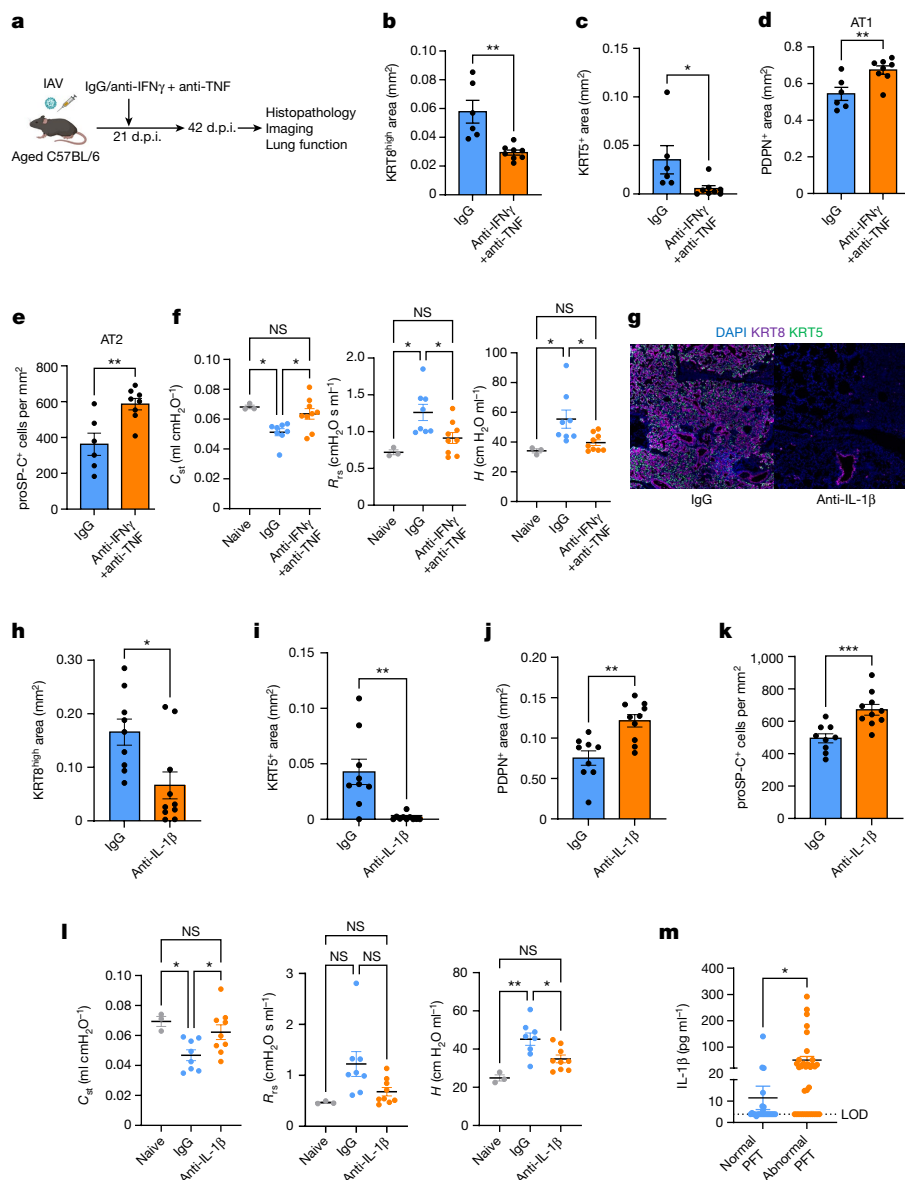
Fig. 5 | Therapeutic neutralization of IFNγ and TNF or IL-1β activity promotes alveolar regeneration and restores lung function. a, The experimental design for in vivo IFNγ + TNF neutralization after IAV infection. The diagram was created using BioRender. **b**−**e**, Quantification of the KRT8^{high} area (**b**; **$P = 0.0017$), KRT5^{+} cell area (**c**; *$P = 0.0404$), AT1 (PDPN[+]) area (**d**; **$P = 0.0073$) and AT2 (proSP-C^{+}) cells per mm[2] (**e**; **$P = 0.0046$) in aged IAV-infected mice treated with anti-IFNγ + anti-TNF neutralizing antibody ($n = 8$) or control IgG antibody ($n = 6$). **f**, Evaluation of static compliance (*$P = 0.0232$ (left) and 0.0217 (right)), resistance of the respiratory system (*$P = 0.0142$ (left) and 0.0282 (right)) and tissue elastance (*H*; *$P = 0.0417$ (left) and 0.0355 (right)) in aged naive ($n = 3$) and IAV-infected mice treated with anti-IFNγ + anti-TNF neutralizing antibody ($n = 9$) or control IgG antibody ($n = 8$). **g**−**k**, Representative immunofluorescence images (**g**) and quantification of KRT8^{high} cell area

(**h**; *$P = 0.0118$), KRT5^{+} cell area (**i**; **$P = 0.0014$), AT1 (PDPN[+]) cell area (**j**; **$P = 0.0011$) and AT2 (proSP-C^{+}) cells per mm[2] (**k**; ***$P = 0.0009$) in aged IAV-infected lung sections treated with anti-IL-1β ($n = 10$) or control IgG ($n = 9$) antibody. **l**, Evaluation of static compliance (*$P = 0.0361$ (left) and 0.0468 (right)), resistance of the respiratory system and tissue elastance (*$P = 0.0244$, **$P = 0.0019$) in aged naive ($n = 3$) or IAV-infected mice treated with anti-IL-1β ($n = 9$) or control IgG ($n = 8$) antibody. **m**, Evaluation of the IL-1β levels in the plasma of convalescent individuals recovering from COVID-19 with or without abnormal lung function ($n = 25$ (normal) and $n = 33$ (abnormal); *$P = 0.0182$). LOD, limit of detection; PFT, pulmonary function test. Data are representative of three (**b**−**f** and **h**−**l**) independent experiments. Statistical analysis was performed using two-tailed unpaired *t*-tests (**b**−**e**, **h**−**k** and **m**) and one-way ANOVA (**f** and **l**). Data are mean ± s.e.m.

remains unclear. However, the prominent spatiotemporal association between the epithelial progenitors and CD8^{+} T cells in post-viral lungs strongly suggests the production of T cell recruitment and/ or survival signals by the epithelium. It is vital to further extend this work and identify the contributions of other immunological factors in the post-viral lung, including interactions with the mesenchyme and the endothelium in dictating the balance between functional and pathological lung repair. Importantly, this model provides a platform to further define mechanisms of post-viral disease that is not confined

to SARS-CoV-2 infection but has also been reported after viral infections such as influenza, MERS-CoV and SARS-CoV-1[2,3].

As PASC and other post-viral pathologies are typically diagnosed several weeks or months after the primary infection, effective treatment strategies to rescue disease in the chronic phase are critical. In contrast to anti-viral agents that require early intervention[10], we show that the neutralization of IFNγ + TNF or IL-1β activity in the post-viral lung can be used as a 'pro-repair' strategy to augment alveolar regeneration and dampen fibrotic sequelae. Our data strongly suggest that drugs such

as anakinra, an IL-1 receptor antagonist, or baricitinib, a JAK inhibitor, may be promising candidates to address this unmet need and treat respiratory PASC[53,54]. Considering that four respiratory viral pandemics and several more epidemics have occurred in the past two centuries, this work may have implications beyond respiratory PASC and could be foundational for potential (and probable) future viral outbreaks.

Online content

Any methods, additional references, Nature Portfolio reporting summaries, source data, extended data, supplementary information, acknowledgements, peer review information; details of author contributions and competing interests; and statements of data and code availability are available at https://doi.org/10.1038/s41586-024-07926-8.

1. Nalbandian, A. et al. Post-acute COVID-19 syndrome. Nat. Med. **27**, 601–615 (2021).
2. Choutka, J., Jansari, V., Hornig, M. & Iwasaki, A. Unexplained post-acute infection syndromes. Nat. Med. **28**, 911–923 (2022).
3. Narasimhan, H., Wu, Y., Goplen, N. P. & Sun, J. Immune determinants of chronic sequelae after respiratory viral infection. Sci. Immunol. **7**, eabm7996 (2022).
4. Cheon, I. S. et al. Immune signatures underlying post-acute COVID-19 lung sequelae. Sci. Immunol. **6**, eabk1741 (2021).
5. Vijayakumar, B. et al. Immuno-proteomic profiling reveals aberrant immune cell regulation in the airways of individuals with ongoing post-COVID-19 respiratory disease. Immunity **55**, 542–556 (2022).
6. Phetsouphanh, C. et al. Immunological dysfunction persists for 8 months following initial mild-to-moderate SARS-CoV-2 infection. Nat. Immunol. **23**, 210–216 (2022).
7. Jyothula, S. S. K. et al. Fulminant lung fibrosis in non-resolvable COVID-19 requiring transplantation. eBioMedicine **86**, 104351 (2022).
8. Gagiannis, D. et al. Clinical, imaging, and histopathological features of pulmonary sequelae after mild COVID-19. Am. J. Respir. Crit. Care Med. **208**, 618–621 (2023).
9. Yao, C. et al. Maladaptive TGF-β signals to the alveolar epithelium drive fibrosis after COVID-19 infection. Am. J. Respir. Crit. Care Med. **208**, 201–204 (2023).
10. Xie, Y., Choi, T. & Al-Aly, Z. Association of treatment with nirmatrelvir and the risk of post–COVID-19 condition. JAMA Intern. Med. **183**, 554–564 (2023).
11. Al-Aly, Z., Xie, Y. & Bowe, B. High-dimensional characterization of post-acute sequelae of COVID-19. Nature **594**, 259–264 (2021).
12. Bharat, A. et al. Lung transplantation for patients with severe COVID-19. Sci. Transl. Med. **12**, eabe4282 (2020).
13. Stewart, I. et al. Residual lung abnormalities after COVID-19 hospitalization: interim analysis of the UKILD Post-COVID-19 Study. Am. J. Respir. Crit. Care Med. **207**, 693–703 (2022).
14. Bowe, B., Xie, Y. & Al-Aly, Z. Postacute sequelae of COVID-19 at 2 years. Nat. Med. **29**, 2347–2357 (2023).
15. Merad, M., Blish, C. A., Sallusto, F. & Iwasaki, A. The immunology and immunopathology of COVID-19. Science **375**, 1122–1127 (2022).
16. Bingham, G. C. et al. High-dimensional comparison of monocytes and T cells in post-COVID and idiopathic pulmonary fibrosis. Front. Immunol. **14**, 1308594 (2024).
17. Arish, M., Qian, W., Narasimhan, H. & Sun, J. COVID-19 immunopathology: from acute diseases to chronic sequelae. J. Med. Virol. **95**, e28122 (2023).
18. Klein, J. et al. Distinguishing features of long COVID identified through immune profiling. Nature **623**, 139–148 (2023).
19. Vaughan, A. E. et al. Lineage-negative progenitors mobilize to regenerate lung epithelium after major injury. Nature **517**, 621–625 (2015).
20. Kobayashi, Y. et al. Persistence of a regeneration-associated, transitional alveolar epithelial cell state in pulmonary fibrosis. Nat. Cell Biol. **22**, 934–946 (2020).
21. Strunz, M. et al. Alveolar regeneration through a Krt8+ transitional stem cell state that persists in human lung fibrosis. Nat. Commun. **11**, 3559 (2020).
22. Choi, J. et al. Inflammatory signals induce AT2 cell-derived damage-associated transient progenitors that mediate alveolar regeneration. Cell Stem Cell **27**, 366–82 (2020).
23. Kumar, P. A. et al. Distal airway stem cells yield alveoli in vitro and during lung regeneration following H1N1 influenza infection. Cell **147**, 525–538 (2011).
24. Xie, T. et al. Abnormal respiratory progenitors in fibrotic lung injury. Stem Cell Res. Ther. **13**, 64 (2022).
25. Habermann, A. C. et al. Single-cell RNA sequencing reveals profibrotic roles of distinct epithelial and mesenchymal lineages in pulmonary fibrosis. Sci. Adv. **6**, eaba1972 (2020).
26. Adams, T. S. et al. Single-cell RNA-seq reveals ectopic and aberrant lung-resident cell populations in idiopathic pulmonary fibrosis. Sci. Adv. **6**, eaba1983 (2020).
27. Rendeiro, A. F. et al. Persistent alveolar type 2 dysfunction and lung structural derangement in post-acute COVID-19. Preprint at medRxiv https://doi.org/10.1101/2022.11.28.22282811 (2022).
28. Jiang, P. et al. Ineffectual type 2-to-type 1 alveolar epithelial cell differentiation in idiopathic pulmonary fibrosis: persistence of the KRT8hi transitional state. Am. J. Respir. Crit. Care Med. **201**, 1443–1447 (2020).
29. Tsukui, T. et al. Collagen-producing lung cell atlas identifies multiple subsets with distinct localization and relevance to fibrosis. Nat. Commun. **11**, 1920 (2020).
30. Leist, S. R. et al. A mouse-adapted SARS-CoV-2 induces acute lung injury and mortality in standard laboratory mice. Cell **183**, 1070–1085 (2020).
31. Dinnon, K. H. SARS-CoV-2 infection produces chronic pulmonary epithelial and immune cell dysfunction with fibrosis in mice. Sci. Transl. Med. **14**, eabo5070 (2022).
32. Goplen, N. P. et al. Tissue-resident CD8+ T cells drive age-associated chronic lung sequelae after viral pneumonia. Sci. Immunol. **5**, eabc4557 (2020).
33. Dinnon, K. H. et al. A mouse-adapted model of SARS-CoV-2 to test COVID-19 countermeasures. Nature **586**, 560–566 (2020).
34. Winkler, E. S. et al. SARS-CoV-2 infection of human ACE2-transgenic mice causes severe lung inflammation and impaired function. Nat. Immunol. **21**, 1327–1335 (2020).
35. Wei, X., Narasimhan, H., Zhu, B. & Sun, J. Host recovery from respiratory viral infection. Ann. Rev. Immunol. **41**, 277–300 (2023).
36. Wang, F. et al. Regulation of epithelial transitional states in murine and human pulmonary fibrosis. J. Clin. Invest. **133**, e165612 (2023).
37. Liang, J. et al. Reciprocal interactions between alveolar progenitor dysfunction and aging promote lung fibrosis. eLife **12**, e85415 (2023).
38. D'Agnillo, F. et al. Lung epithelial and endothelial damage, loss of tissue repair, inhibition of fibrinolysis, and cellular senescence in fatal COVID-19. Sci. Transl. Med. **13**, eabj7790 (2021).
39. Melms, J. C. et al. A molecular single-cell lung atlas of lethal COVID-19. Nature **595**, 114–119 (2021).
40. Konkimalla, A. et al. Transitional cell states sculpt tissue topology during lung regeneration. Cell Stem Cell **30**, 1486–502 (2023).
41. Fiege, J. K. & Langlois, R. A. Investigating influenza A virus infection: tools to track infection and limit tropism. J. Virol. **89**, 6167–6170 (2015).
42. Katsura, H., Kobayashi, Y., Tata, P. R. & Hogan, B. L. M. IL-1 and TNFα contribute to the inflammatory niche to enhance alveolar regeneration. Stem Cell Rep. **12**, 657–666 (2019).
43. Kostura, M. J. et al. Identification of a monocyte specific pre-interleukin 1 beta convertase activity. Proc. Natl Acad. Sci. USA **86**, 5227–5231 (1989).
44. Littlefield, K. M. et al. SARS-CoV-2-specific T cells associate with inflammation and reduced lung function in pulmonary post-acute sequalae of SARS-CoV-2. PLoS Pathog. **18**, e1010359 (2022).
45. Krishna, B. A. et al. Spontaneous, persistent, T cell-dependent IFN-γ release in patients who progress to long COVID. Sci. Adv. **10**, eadi9379 (2024).
46. Riemondy, K. A. et al. Single cell RNA sequencing identifies TGFβ as a key regenerative cue following LPS-induced lung injury. JCI Insight **5**, e123637 (2019).
47. Nabhan, A. N., Brownfield, D. G., Harbury, P. B., Krasnow, M. A. & Desai, T. J. Single-cell Wnt signaling niches maintain stemness of alveolar type 2 cells. Science **359**, 1118–1123 (2018).
48. Salama, C. et al. Tocilizumab in patients hospitalized with COVID-19 pneumonia. N. Engl. J. Med. **384**, 20–30 (2020).
49. Stancil, I. T. et al. Interleukin-6-dependent epithelial fluidization initiates fibrotic lung remodeling. Sci. Transl. Med. **14**, eabo5254 (2022).
50. Choi, J. et al. Release of Notch activity coordinated by IL-1β signalling confers differentiation plasticity of airway progenitors via Fosl2 during alveolar regeneration. Nat. Cell Biol. **23**, 953–966 (2021).
51. Chen, B., Julg, B., Mohandas, S., Bradfute, S. B. & Force RMPT. Viral persistence, reactivation, and mechanisms of long COVID. eLife **12**, e86015 (2023).
52. Proal, A. D. et al. SARS-CoV-2 reservoir in post-acute sequelae of COVID-19 (PASC). Nat. Immunol. **24**, 1616–1627 (2023).
53. An EUA for baricitinib (olumiant) for COVID-19. Med. Lett. Drugs Ther. **62**, 202–203 (2020).
54. An EUA for anakinra (kineret) for COVID-19. Med. Lett. Drugs Ther. **64**, e203 (2022).

Article

Methods

Ethics and biosafety

All aspects of this study were approved by the Institutional Review Board Committee at Cedars-Sinai Medical Center (IRB Pro00035409) and the University of Virginia (IRB 13166). Work related to SARS-CoV-2 was performed in animal biosafety level 3 (ABSL-3) facilities at the University of Virginia and influenza-related experiments were performed in animal biosafety level 2 (ABSL-2) facilities at the Mayo Clinic and the University of Virginia.

Cells, viruses and mice

The African green monkey kidney cell line Vero E6 (ATCC CRL-1587) was obtained from ATCC, tested to be free of mycoplasma contamination and maintained in Dulbecco's modified Eagle's medium (DMEM) supplemented with 10% fetal bovine serum (FBS), along with 1% penicillin–streptomycin and L-glutamine at 37 °C in 5% CO_2. The SARS-CoV-2 mouse-adapted strain (MA-10) was provided by B. J. Mann. The virus was passaged in Vero E6 cells, and the titre was determined by plaque assay using Vero E6 cells.

Young (aged 8–10 weeks) and aged (aged 84 weeks) female C57BL/6J mice, and 15-week-old female BALB/cJ mice (aged in-house to 10–12 months) were purchased from The Jackson Laboratory (JAX). K18-hACE2 (034860) transgenic mice as well as wild-type C57BL/6 (000664) mice were purchased from the Jackson Laboratory and bred in-house. Aged mice were received at 20 to 21 months of age from the National Institutes of Aging and all mice were maintained in the facility for at least 1 month before infection. All of the mice were housed in a specific-pathogen-free environment and used under conditions fully reviewed and approved by the institutional animal care and use committee guidelines at the Mayo Clinic (Rochester, MN) and University of Virginia (Charlottesville, VA).

For primary IAV virus infection, influenza A/PR8/34 strain (75 plaque-forming units (PFU) per mouse) was diluted in fetal bovine serum (FBS)-free Dulbecco's modified Eagle's medium (DMEM) (Corning) on ice and inoculated in anesthetized mice through intranasal route as described previously[32]. For SARS-CoV-2 infections, mice were infected with 5×10^4 PFU for C57BL/6 and 1,000 PFU for BALB/c of mouse-adapted (MA-10) virus or 200 PFU of USA-WA1/2020 for K18-hACE2 mice, intranasally under anaesthesia as described previously. Infected mice were monitored daily for weight loss and clinical signs of disease for 2 weeks, and later once a week for the duration of the experiments. The mortality rate of mice was calculated from mice that were either found dead in the cage or were euthanized when they reached 70% of their starting body weight, which is the defined humane end point in accordance with the respective institutional animal protocols. At the designated end point, the mice were humanely euthanized by ketamine–xylazine overdose and subsequent cervical dislocation. For this study, animal numbers were estimated on the basis of previous results from our infection model. Mice were assigned to treatment groups accounting for equal distribution of severity of acute disease across groups and thus investigators were not blinded to group allocation.

In vivo drug treatment

For depletion of CD8+ T cells and neutralization of cytokines, starting at 21 d.p.i., mice were intraperitoneally administered 20 μg or 500 μg of anti-CD8 antibody (53-6.7 and 2.43; BioXCell), anti-IL-1β (B122; BioX-Cell), anti-IFNγ (XMG1.2; BioXCell), anti-TNF (XT3.11; BioXCell) or isotype control immunoglobulin G (IgG) in 200 μl PBS once a week. Mice were euthanized 3 days after the last treatment.

Evaluation of respiratory mechanics and lung function

Lung function measurements using the forced oscillation technique and the resulting parameters have been previously described[55]. In brief, animals were anaesthetized with an overdose of ketamine–xylazine (100 and 10 mg per kg intraperitoneally) and paralysed with pancuronium bromide (1mg per kg intraperitoneally) to prevent respiratory efforts. Mice were then tracheostomized with a blunt 18-gauge canula (typical resistance of 0.18 cm H_2O s ml^{-1}), which was secured in place with a nylon suture. The mice were connected to the computer-controlled piston (SCIREQ flexiVent), and forced oscillation mechanics were performed under tidal breathing conditions described previously[55] with a positive-end expiratory pressure of 3 cm H_2O. The measurements were repeated after thorough recruitment of closed airways (two manoeuvres rapidly delivering total lung capacity of air and sustaining the required pressure for several seconds, mimicking holding of a deep breath). Each animal's basal conditions were normalized to their own maximal capacity. Measurement of these parameters before and after lung inflation enables determination of large and small airway dysfunction under tidal (baseline) breathing conditions. Only measurements that satisfied the constant-phase model fits were used (>90% threshold determined by software). After this procedure, mice had a heart rate of around 60 beats per minute, indicating that the measurements were carried out on live individuals.

Human lung tissue specimens

Human lung samples were obtained from patients enrolled in the IRB-approved Lung Institute BioBank (LIBB) study at Cedars-Sinai Medical Center, Los Angeles, CA and at the University of Virginia, Charlottesville, VA. All of the participants or their legal representatives provided informed written consent. Lung tissues were processed within 24 h after surgical removal. Specifically, the lung tissues were cut and immediately fixed in 10% normal-buffered formalin for 24 h before tissue processing using the HistoCore PEARL–Tissue Processor (Leica) and embedding in paraffin for histological studies. The formalin-fixed paraffin-embedded cassettes were appropriately stored at room temperature until further sectioning.

For the influenza samples, lungs from deceased donors were obtained during organ acquisition for clinical transplantation through LifeLink of Georgia. As the donors were deceased at the time of collection, this study was exempt from International Review Board review. Informed consent was obtained from next of kin before explant. To ensure tissue viability, the samples were transported on ice and processed within 12 h of procurement. The sections from the human lungs were cut, embedded in OCT and then flash-frozen for immunofluorescence microscopy.

Mouse tissue processing and flow cytometry analysis

Mice were injected intravenously with 2 μg of CD45 or CD90.2 antibody labelled with various fluorochromes. Then, 2 min after injection, the mice were euthanized with an overdose of ketamine–xylazine and processed 3 min later. After euthanasia, the right ventricle of the heart was gently perfused with chilled 1× PBS (10 ml). The right lobes of the lungs were collected in 5 ml of digestion buffer (90% DMEM and 10% PBS and calcium with type 2 collagenase (180 U ml^{-1}; Worthington) and DNase (15 μg ml^{-1}; Sigma-Aldrich) additives). Tissues were digested at 37 °C for 1 h followed by disruption using the gentleMACS tissue dissociator (Miltenyi). Single-cell suspensions were obtained by hypotonic lysis of red blood cells in ammonium-chloride-potassium buffer and filtration through a 70 μm mesh. Cells were washed with FACS buffer (2% of FBS and 0.1% of NaN_3 in PBS) and FCγ receptors were blocked with anti-CD16/32 (2.4G2). Surface staining was performed by antibody (details of which are provided in Supplementary Table 5) incubation for 30 min at 4 °C in the dark. After washing with PBS, cells were resuspended with Zombie-dye (BioLegend) and incubated at room temperature for 15 min. For IL-1β staining, cells were incubated with monesine (BioLegend) for 5 h at 37 °C and then stained with surface markers antibodies. After washing with FACS buffer, cells were fixed with fixation buffer (BioLegend) and permeabilized with intracellular staining permeabilization wash buffer (BioLegend). The cells were then

stained with anti-IL-1β at room temperature for 1 h and the samples were acquired on the Attune NxT (Life Technologies) system. The data were analysed using Attune NXT software (v.5.2.0) and FlowJo (Tree Star).

Caspase-1 FLICA analysis
Caspase-1 was detected using the FAM-FLICA Caspase-1 Assay Kit (ImmunoChemistry Technologies) according to the manufacturer's instructions. In brief, lung single cells or macrophages from in vitro culture were stained with fluorochrome-conjugated antibody cocktail for cell surface markers. After staining, cells were incubated with FLICA for 30 min at 37 °C, washed and detected by flow cytometry.

Cell isolation and ex vivo co-culture
To isolate myeloid and CD8+ T cells, single-cell suspension of the lung was generated from IAV-infected mice as described above and labelled and enriched with CD11c and CD11b or CD8 microbeads (Miltenyi Biotec) according to the manufacturer's instructions. Purified myeloid cells were seeded in 96-well (200,000 per well) plates and incubated for 2 h at 37 °C 5% CO_2 to facilitate attachment. Wells were washed with 1× PBS to select for macrophages, following which selected wells were seeded with naive or memory CD8+ T cells (40,000 per well) and further incubated for 16–18 h. Supernatant and cell pellets were collected for cytokine measurement and gene expression analyses, respectively.

AT2 cell isolation and culture
AT2 cells were isolated from naive mice as previously described[46,56,57]. In brief, mouse lungs were perfused with chilled PBS and intratracheally instilled with 1 ml of dispase II (15 U ml^{-1}, Roche), tying off the trachea and cutting away the lobes from the mainstem bronchi. Lungs were incubated in 4 ml of 15 U ml^{-1} dispase II for 45 min while shaking at room temperature, followed by mechanical dissociation with an 18 G needle. After passage through a 100 µm filter, lungs underwent 10 min of DNase I digestion (50 µg ml^{-1}) and were filtered through a 70 µm filter before RBC lysis. Single-cell suspensions were subjected to CD45 depletion using microbeads (Miltenyi), incubated with anti-FcgRIII/II (Fc block) and stained for CD45, EPCAM and MHC-II, and with viability die (antibody details are provided in Supplementary Table 5). Fluorescence-activated cell sorting was performed on the BD Influx cell sorter to isolate AT2 cells as described previously[56] and collected in 500 µl DMEM + 40% FBS + 2% penicillin–streptomycin. Sorted AT2 cells (200,000 per well) were plated in a 96-well plate in DMEM/F12 + 10% FBS and cultured at 37 °C, 5% CO_2 for 3 days before collection. For in vitro neutralization, anti-IL-1β (B122; BioXCell) was used at 10 µg ml^{-1} and, for stimulation, IL-1β (Peprotech) was used at 20 ng ml^{-1}.

RNA isolation and qPCR with reverse transcription
Cells were lysed in buffer RLT and RNA was purified using the RNeasy Plus Mini Kit (Qiagen) according to the manufacturer's instructions. Random primers (Invitrogen) and MMLV reverse transcriptase (Invitrogen) were used to synthesize first-strand complementary DNAs (cDNAs) from equivalent amounts of RNA from each sample. cDNA was used for quantitative PCR (qPCR) with the Fast SYBR Green PCR Master Mix (Applied Biosystems). qPCR was conducted on the QuantStudio 3 (Applied Bioscience) system. Data were generated with the comparative threshold cycle (ΔC_t) method by normalizing to hypoxanthine-guanine phosphoribosyltransferase (*HPRT*) transcripts in each sample as reported previously[58].

COVID-19 convalescent cohort
Peripheral blood specimens were obtained from patients presenting to the University of Virginia Post-COVID-19 clinic. All of the participants provided written informed consent. Pulmonary function testing (spirometry, lung volume testing, diffusing capacity of the lungs for carbon monoxide) at the time of blood draws was used to define normal and abnormal lung function.

IL-1β cytokine evaluation
Plasma from convalescent individuals recovering from COVID-19, supernatant from ex vivo culture and mouse BAL fluid after flushing of airway with 600 µl of sterile PBS were used to quantify IL-1β levels by ELISA according to the manufacturer's instructions (R&D systems). The samples were first concentrated 5× (BAL) and 2× (cell culture supernatant) using Microcon-10kDa centrifugal filters (Millipore Sigma).

Histopathological analysis of lung tissues
Mouse lungs were routinely perfused with ice cold 1× PBS and the left lung was inflated and fixed in 10% formalin, embedded in paraffin and cut into 5-µm-thick sections. The sections were stained with haematoxylin–eosin and Masson's trichrome. All of the sections were studied using light microscopy. The severity of fibrosis was semi-quantitatively assessed by blinded reviewers according to a modified Ashcroft scale[59] and scored between 0 to 8 by examining randomly chosen fields. For histopathology, tissues were evaluated for oedema or hyaline membranes, interstitial disease and perivascular infiltrates as previously described[60].

Immunofluorescence
Formalin-fixed paraffin-embedded lung tissue sections (5 µm) were deparaffinized in xylene and rehydrated. For PDLIM7 staining, tissues were fixed in 4% PFA at 4 °C for 8 h before cryoprotection in 30% sucrose. Tissues were later embedded in OCT and sectioned (5 µm). Heat-induced antigen retrieval was performed using 1× Agilent Dako target retrieval solution (pH 9) or 1× citrate solution (for frozen tissue; pH 6) in a steamer for 20 min (mouse lungs) or 45 min (human lungs), followed by blocking and surface staining. For intracellular targets, tissues were permeabilized with 0.5% Triton X-100 and 0.05% Tween-20 for 1 h at room temperature. The sections were stained with primary antibodies as listed in Supplementary Table 5 overnight at 4 °C. Subsequently, the samples were washed and incubated with fluorescent secondary antibodies as listed in Supplementary Table 5 for 2 h at room temperature. The sections were counterstained with DAPI (1:1,000, Thermo Fisher Scientific) for 3 min and mounted using ProLong Diamond Antifade mountant (Thermo Fisher Scientific). After 24 h of curing at room temperature, images were acquired using a ×10 or ×20 objective on the Olympus BX63 fluorescence microscope and pseudo-colours were assigned for visualization. For all mouse samples, the left lobe of the lungs was used for imaging, for which 10–12 random fields in the distal lung were considered for quantification and the average value from each mouse was represented in respective graphs. Human lungs were similarly imaged and quantified; however, all available lobes sections were used. All images were further processed using ImageJ Fiji, cellSens, OlyVIA and/or QuPath software[61]. Quantitative analysis of stitched immunofluorescence images was performed using QuPath v.0.4.1, where tissue-specific expression of KRT8^{high} was used to annotate areas of dysplastic repair and discriminate them from the remaining intact human or mouse lung tissue. CD8+ T cells and macrophages were detected using CD8α or CX3CR1 (mouse)/CD68 (human) signals, respectively. The abundance and distribution of the respective cells of interest were quantified to plot the distance from the annotation (KRT8^{high}). Density maps were further generated to identify hotspots of the cells across the tissue with respect to the annotations. The same parameters for annotation and cell type classification were applied to all of the samples from the same experiment.

RNA in situ hybridization
RNA in situ hybridization was performed on paraffin-embedded lung sections using the RNAscope Multiplex Fluorescent Assay v2 according to the manufacturer's instructions (Advanced Cell Diagnostics; ACD). Tissues were deparaffinized with xylene (2×, 5 min) and 100% ethanol (2×, 2 min) and incubated with hydrogen peroxide for 10 min

Article

at room temperature. Using a steamer, target retrieval was performed for 30 min followed by 30 min treatment with Protease Plus (ACD) at 40 °C. The slides were hybridized with custom probes at 40 °C for 2 h and signals were amplified according to the manufacturer's instructions. Stained sections were captured at ×20 using the Olympus BX63 fluorescence microscope.

ST analyses

Spatial transcriptomics (ST) data (generated on the 10x Visium platform) were preprocessed using the spaceranger package (v.2.0, genome version mm10). The R package Seurat (v.4.3.0) was used for quality control and basic analyses. Only high-quality spots with sufficient gene coverage (≥2,000) were retained for downstream analysis. Similar to the single-cell RNA-sequencing data, the spatial expression data were first normalized to a log scale using the SCTransform method (v.0.3.5). The top 2,000 highly variable genes were then identified based on the variance of expression across spots for the principal component analysis input. UMAP embeddings were generated for visualization at the reduced dimensionality (top 30 principal components). Spots were clustered with a shared nearest neighbour modularity optimization-based clustering algorithm (built in Seurat). The samples were integrated and batch-effects were removed using the Harmony package (v.0.1). In addition to the spatial spot view of the expression pattern, we used UMAP to visualize the expression pattern of spots associated with the identified cell types in a lower dimension using the visualization pipeline in the Seurat package. Marker gene (differentially expressed genes (DEGs)) detection among different groups of spots was also performed with Seurat (FindMarker function), and the marker gene lists were further submitted to the gene set enrichment analysis pre-rank test for the functional annotation analysis.

We determined each spot's potential cell type composition based on the following protocol. (1) We define alveolar epithelium (AE) spots based on the k-means clustering analysis (using knowledge-based key genes from different cell types). (2) For non-AE spots, we use the average expression of the Krt marker gene list (Supplementary Table 6) to estimate a Krt score and, similarly, average expression of Cd8 marker gene list (Supplementary Table 6) for Cd8 score. We set −0.4 as the cut-off for both the Cd8 and Krt score: spots with a Krt/Cd8 score > −0.4 were assigned as a Krt/Cd8-associated spot, and assigned blue/red colour, respectively, in the spatial map. Thus, a spot can exhibit a Krt and Cd8 signature at the same time, and we use purple to represent this category (Fig. 3a). For a given gene list, we captured the expression of relevant genes to compare the distribution of their expression index between Krt spots and AE spots. The significance of the difference was estimated using the Wilcoxon rank-sum test. The P values were then $\log_{10}$ transformed and displayed as bar plots. Similar to the Cd8 score and Krt score, we also defined some other cell type scores based on our knowledge-based marker gene list (Supplementary Table 6). We further used these scores to estimate the association between cell types in a specific slide or the global level (Pearson correlation coefficient). A pair of cell types with a higher Pearson correlation coefficient between their cell type score indicates a higher likelihood of their co-occurrence within the same spots.

For human ST data, most analyses were performed using methods similar to the mouse ST data. Moreover, we split spots by the expression of *KRT8* and *AGER* using the cut-off of normalized expression index greater than 4. Spots with *KRT8* > 4 and *AGER* ≤ 4 were defined as *KRT8*-only spots, whereas spots with *KRT8* ≤ 4 and *AGER* > 4 were defined as *AGER*-only spots. These two spot sets were collected to compare the difference in cell type scores, key gene expression and pathway enrichment between them. In detail, we compared the percentage of ON spots (given a cell type score or gene expression index passing the cut-off) between the two groups (for example, *KRT17*-only spots versus *AGER*-only spots, or COVID spots versus control spots), and displayed the results as bar plots. A similar analysis was applied to examine the

enrichment of relevant signalling pathways. Note that the cut-offs of normalized single-gene expression were set to 0.8. The cell type score (for example, CD8, KRT, AE, MDM and AM scores) was set to 1.2 for human data, as the distribution of marker gene expression varied between different species and biological samples (that is, human lung COVID samples). Detailed marker gene lists for cell types and pathways are provided in Supplementary Table 6.

To evaluate the similarity between our human and mouse models, we first detected the DEGs between all PASC-PF spots and control spots (using the human ST data). Next, we projected the COVID > control DEGs to identify mouse homologues and compared the expression of these genes in mouse spot categories (for example, IgG versus anti-CD8, or mouse Krt spots versus AE spots). Similarly, we also made this comparison for the DEGs between human KRT spots and AE spots, as well as genes from the top pathways enriched in PASC-PF spots. Wilcoxon rank-sum tests were conducted to evaluate the significance of the difference in expression. The human–mouse homologue information was downloaded from Mouse Genome Informatics (https://www.informatics.jax.org/).

Statistical analyses

Quantitative data are presented as mean ± s.e.m. Unpaired two-tailed Student's t-tests (two-tailed, unequal variance) were used to determine statistical significance with Prism software (GraphPad) for two-group comparison. For multiple-groups comparisons, ANOVA corrected for multiple comparisons was used when appropriate (GraphPad). log-rank (Mantel–Cox) tests were used for survival curve comparison and two-way ANOVA was used to analyse differences in weight loss. $P < 0.05$ was considered to be significant in all statistical tests.

Reporting summary

Further information on research design is available in the Nature Portfolio Reporting Summary linked to this article.

Data availability

All relevant raw data have been deposited at the GEO under accession codes GSE267226 and GSE267228. Source data are provided with this paper.

Code availability

Relevant code used for analysis of human and mouse spatial transcriptomics data has been deposited at GitHub (https://github.com/zang-lab/covidSTanalysis).

55. Goplen, N. et al. Combined sensitization of mice to extracts of dust mite, ragweed, and *Aspergillus* species breaks through tolerance and establishes chronic features of asthma. *J. Allerg. Clin. Immunol.* **123**, 925–932 (2009).
56. Major, J. et al. Endothelial AHR activity prevents lung barrier disruption in viral infection. *Nature* **621**, 813–820 (2023).
57. Weiner, A. I. et al. ΔNp63 drives dysplastic alveolar remodeling and restricts epithelial plasticity upon severe lung injury. *Cell Rep.* **41**, 111805 (2022).
58. Huang, S. et al. PPAR-γ in macrophages limits pulmonary inflammation and promotes host recovery following respiratory viral infection. *J. Virol.* **93**, e00030-19 (2019).
59. Hübner, R. H. et al. Standardized quantification of pulmonary fibrosis in histological samples. *Biotechniques.* **44**, 507–511 (2008).
60. Wong, L.-Y. R. et al. Eicosanoid signalling blockade protects middle-aged mice from severe COVID-19. *Nature* **605**, 146–151 (2022).
61. Bankhead, P. et al. QuPath: open source software for digital pathology image analysis. *Sci. Rep.* **7**, 16878 (2017).

Extended Data Fig. 1 | See next page for caption.

Extended Data Fig. 1 | Spatial transcriptomics of human PASC-PF lungs reveal persistent defects in alveolar regeneration and chronic inflammation.
(a) Representative RNA-ISH images staining for SARS-CoV-2 Spike RNA in acute COVID-19 (n = 5) and PASC-PF lung (n = 18) sections. (b) Representative H&E images of human control and PASC-PF lungs. (Scale bar = 2 mm) (c) UMAP visualization of spatial transcriptomics data from human control (n = 2) and PASC-PF (n = 3) lungs. (d) Gene expression distribution across all identified clusters of spots. (e) GSEA analysis of signalling pathways differentially regulated between control (n = 2) and PASC-PF (n = 3) lungs. (f) Spatial gene expression maps of epithelial and immune cell markers in control (n = 2) and PASC-PF (n = 3) lungs. (g) Spatial gene expression maps of *CD4* in control (n = 2) and PASC-PF (n = 3) lungs. (h) Heatmap of the physical distribution of alveolar epithelium, dysplastic progenitors, and CD8+ T cells. (i) Representative immunofluorescence images staining alveolar epithelial cell markers (AT1 – AGER; AT2 – proSP-C) in control and PASC-PF lung sections, and (j) staining CD8+ T cells (CD8α+) and epithelial progenitors (KRT5+, KRT17+, and KRT^{high}) in control and (k) PASC-PF lung sections. (l) Higher magnification inset of PASC-PF lungs showing independent channels (red arrows – KRT5+, yellow arrows – KRT17+KRT5−,

grey arrows – KRT8^{high}). (m) Quantification of KRT5+ area in control and PASC-PF lung sections (n = 12 control, 8 PASC-PF) (***p = 0.0007). (n) Representative immunofluorescence images staining for myofibroblasts (αSMA) and aberrant epithelial progenitors (KRT5+, KRT17+KRT5−, KRT8^{high}) in human control, PASC-PF, and IPF lung sections. (o) Representative immunofluorescence images staining CD8+ T cells and epithelial progenitors in idiopathic pulmonary fibrosis (IPF) lung sections. (p) Quantification of CD8+ T cell number in control, PASC-PF, and IPF lung sections (n = 11 control, 13 IPF, 19 PASC-PF) (*p = 0.0343; ***p = 0.0001). (q) Representative Masson's Trichome (MT) image (Scale bar = 2 mm) and (r) immunofluorescence images staining alveolar epithelial cell markers (AT1 – AGER; AT2 – proSP-C) in influenza-infected human lung sections. (s) Quantification of AT1 (AGER+) (*p = 0.0261) and AT2 (proSP-C+) (*p = 0.0272) cells, and (t) representative immunofluorescence images staining CD8+ T cells (CD8α+) and KRT8^{high} transitional cells in influenza-infected human lungs (n = 3 control, 4 influenza). Statistical analyses were conducted using a two-tailed unpaired t-test (m,s) and one-way ANOVA (p). *p < 0.05; ***p < 0.001. Data are expressed as mean ± SEM; ns – not significant.
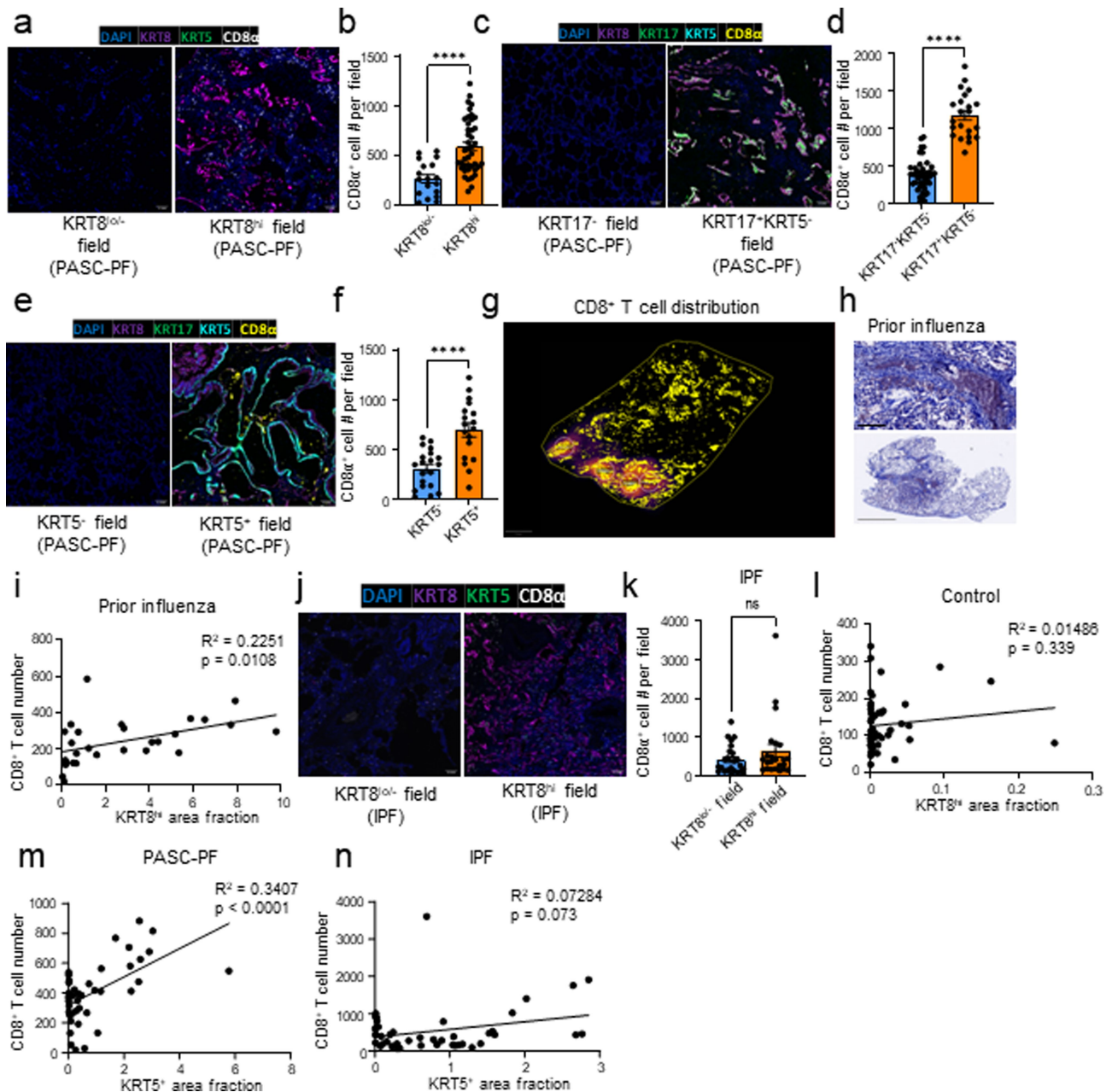
Extended Data Fig. 2 | Characterization of immune-epithelial progenitor interactions in human PASC-PF, influenza, and IPF lungs. (a) Representative immunofluorescence images staining CD8+ T cells and **(b)** quantification of CD8+ T cell distribution within KRT8$^{-/low}$ and KRT8^{high} areas in PASC-PF lungs (5-7 random fields/lung; n = 10) (****p < 0.0001). **(c)** Representative immunofluorescence images staining CD8+ T cells and **(d)** quantification of CD8+ T cell distribution within KRT17−KRT5− or KRT17+KRT5− areas in PASC-PF lungs (5-7 random fields/lung; n = 10) (****p < 0.0001). **(e)** Representative immunofluorescence images staining CD8+ T cells and **(f)** quantification of CD8+ T cell distribution within in KRT5− and KRT5+ areas in PASC lungs (5-7 random fields/lung; n = 10 lungs) (****p < 0.0001). **(g)** Unbiased analysis of CD8+ T cell distribution in an influenza-infected human lung section using

QuPath. **(h)** Representative Masson's Trichrome images of lungs from donors with prior influenza infection. (Scale bar – black = 500 μm; grey = 2 mm). **(i)** Simple linear regression of CD8+ T cell number and KRT8^{high} area fraction in lungs with prior influenza infection (15 random fields/lung; n = 2 lungs). **(j)** Representative immunofluorescence images staining CD8+ T cells and **(k)** quantification of CD8+ T cells in KRT8$^{-/low}$ and KRT8^{high} areas within IPF lungs. (n = 8) **(l-m)** Simple linear regression of CD8+ T cell number and (l) KRT8^{high} area fraction in control lungs (n = 6-8 random fields; N = 7 lungs), **(m)** KRT5+ area fraction in PASC-PF (6-8 random fields/lung; n = 7) and **(n)** KRT+ area fraction in IPF (6-8 random fields/lung; n = 7) lung sections. Statistical analyses were conducted using a two-tailed unpaired t-test. ****p < 0.0001. Data are expressed as mean ± SEM; ns – not significant.
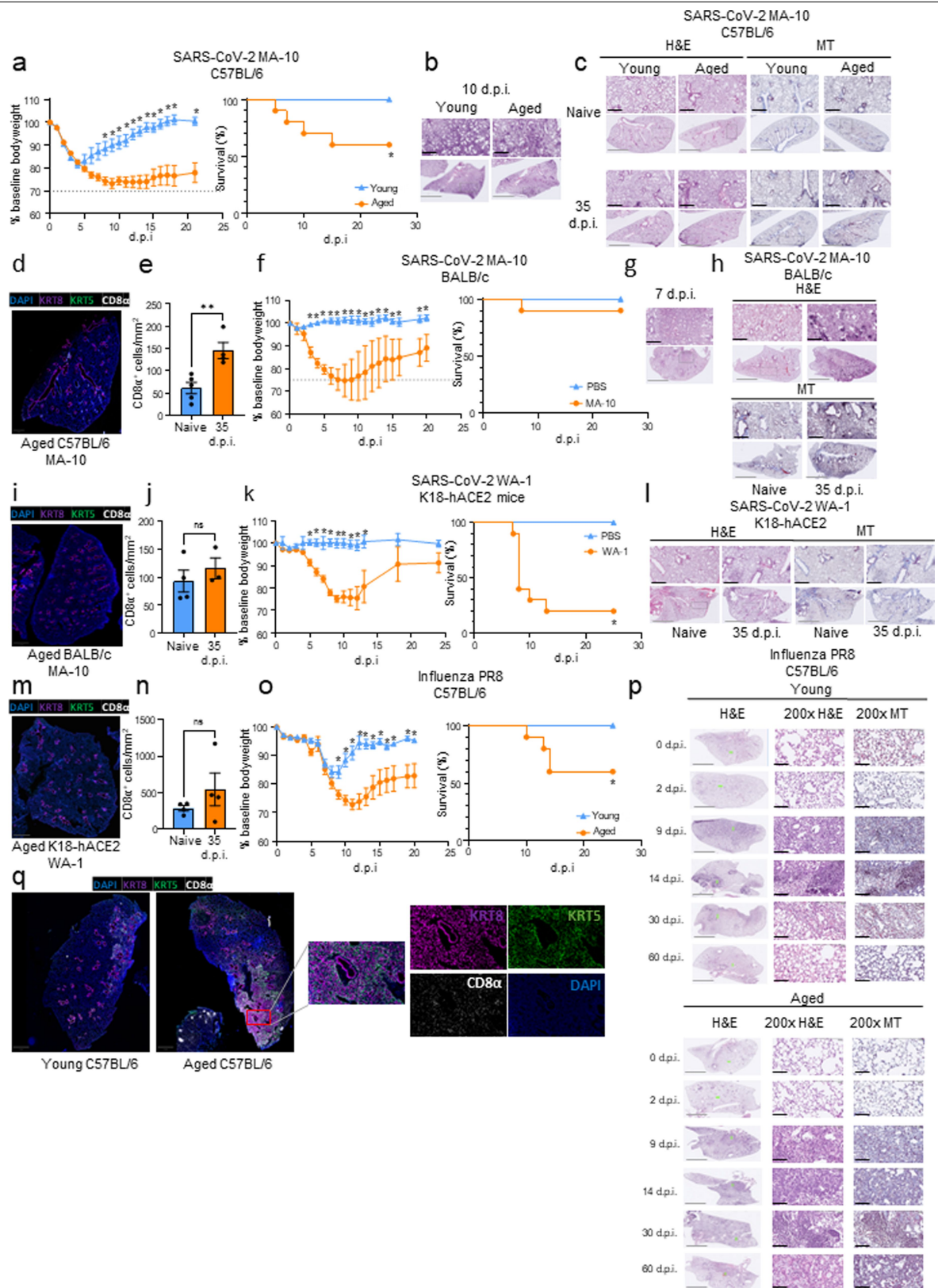
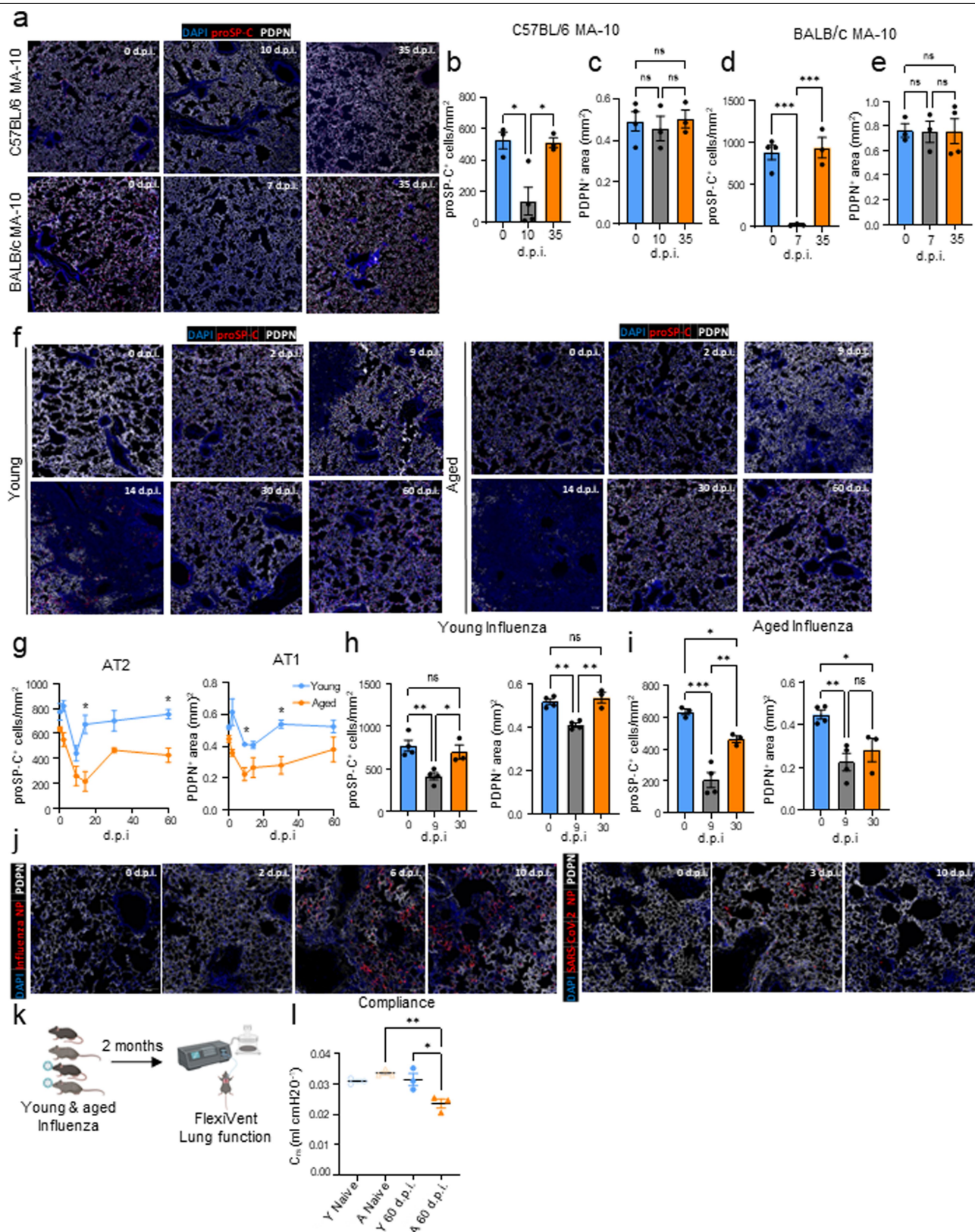**Extended Data Fig. 3** | See next page for caption.

Article

Extended Data Fig. 3 | IAV but not SARS-CoV-2 infection induces chronic pulmonary pathology in aged mice. (a) Percent change in bodyweight and survival (*p = 0.0291) of young and aged C57BL/6 following SARS-CoV-2 MA-10 infection (n = 10 per group). **(b)** Representative H&E images of young and aged C57BL/6 mice from acute (10 d.p.i.), and **(c)** H&E and MT at chronic (35 d.p.i.) phase post SARS-CoV-2 MA-10 infection. **(d)** Representative immunofluorescence images staining CD8+ T cells (CD8α) and epithelial progenitors (KRT5+ and KRT8high), and **(e)** quantification of CD8+ T cells in naïve and SARS-CoV-2 MA-10 infected (35 d.p.i.) aged C57BL/6 lungs. (n = 5 naïve, 4 MA-10) (**p = 0.0058). **(f)** Percent change in bodyweight and survival of aged BALB/c following SARS-CoV-2 MA-10 infection (n = 10 per group). **(g)** Representative H&E images of aged BALB/c mice from the acute (7 d.p.i.), and **(h)** H&E and MT chronic (35 d.p.i.) phase post SARS-CoV-2 MA-10 infection. **(i)** Representative immunofluorescence images staining CD8+ T cells (CD8α) and epithelial progenitors (KRT5+ and KRT8high), and **(j)** quantification of CD8+ T cells in naïve and SARS-CoV-2 MA-10 infected (35 d.p.i.) aged BALB/c lungs. (n = 4 naïve, 3 MA-10) **(k)** Percent change in bodyweight and survival data

(*p = 0.0325) of aged K18-hACE2 mice following SARS-CoV-2 WA-1 virus infection (n = 3 PBS, n = 16 WA-1). **(l)** Representative H&E and MT images of aged K18-hACE2 lungs post SARS-CoV-2 WA-1 infection (35 d.p.i.) or PBS administration. **(m)** Representative immunofluorescen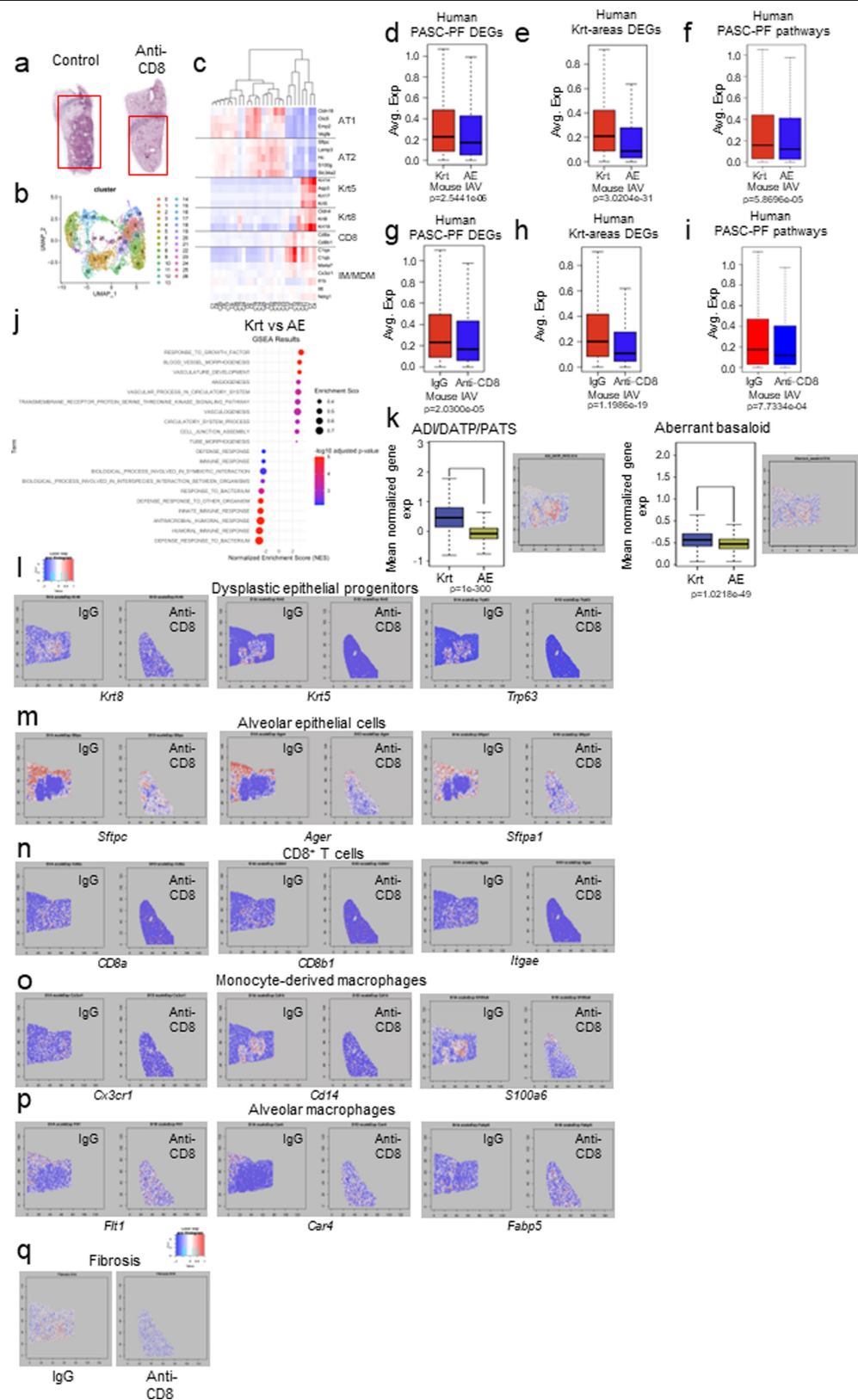ce image staining CD8+ T cells (CD8α) and epithelial progenitors (KRT5+ and KRT8high), and **(n)** quantification of CD8+ T cells in naïve and SARS-CoV-2 WA-1 infected (35 d.p.i.) aged K18-hACE2 mice (n = 4 naïve, 4 WA-1). **(o)** Percent change in bodyweight and survival (*p = 0.0295) data of young and aged C57BL/6 following IAV virus infection (n = 10 per group). **(p)** Representative H&E and MT images of young and aged C57BL/6 lungs post IAV virus infection. **(q)** Representative image of young and aged IAV-infected mouse (35 d.p.i.) lung staining for CD8+ T cells and dysplastic progenitors (KRT8+ and KRT5+). Scale bar – black = 500 μm; grey = 2 mm. Data are representative of two (**a-n**) or three (**o-p**) independent experiments. Statistical analyses were conducted using a two-tailed unpaired t-test (**e,j,n**), two-way ANOVA (BW data – **a,f,k,o**), and log-rank test (survival data - **a,f,k,o**) *p < 0.05; **p < 0.01. Data are expressed as mean ± SEM; ns – not significant.
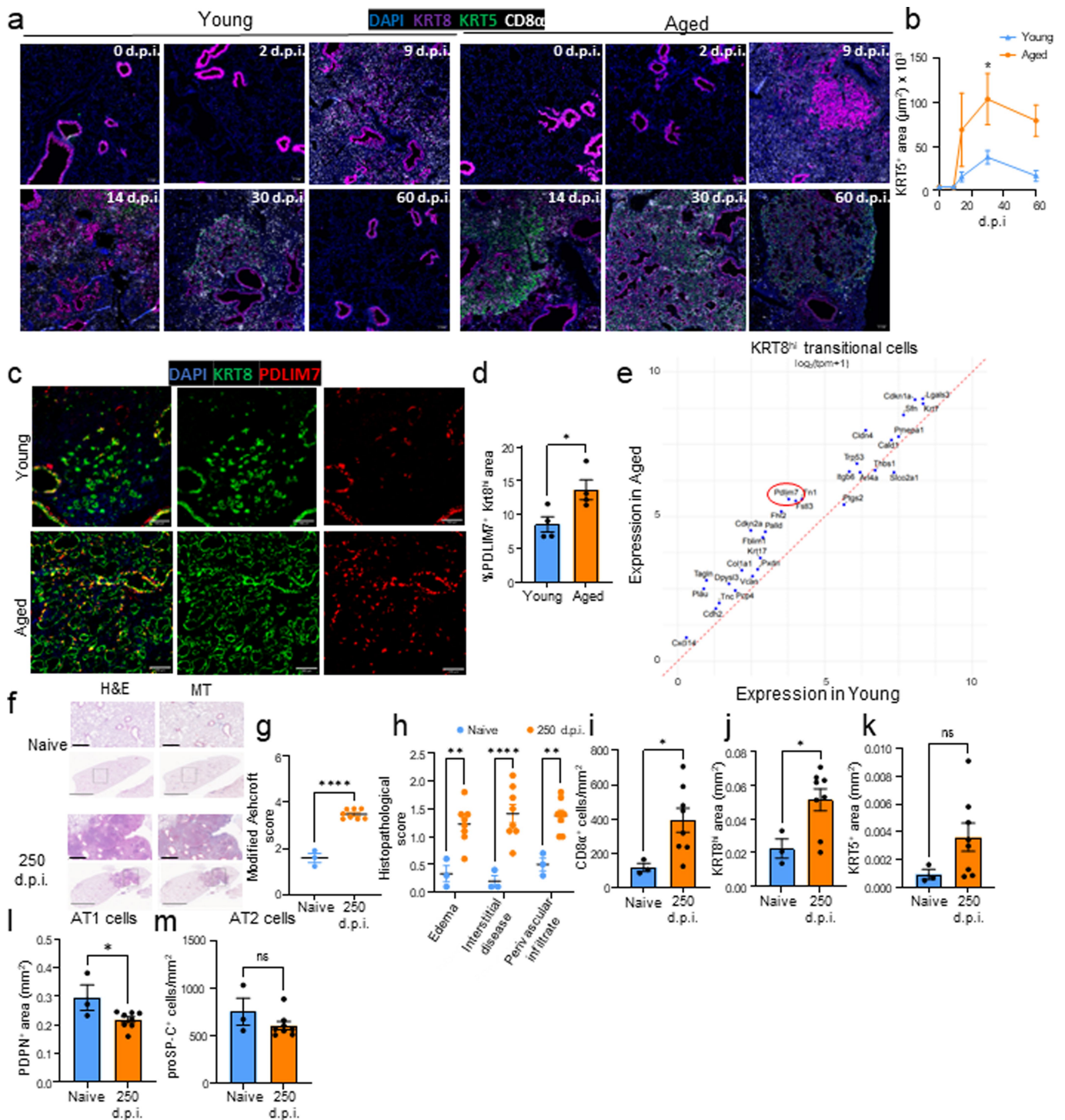
Extended Data Fig. 4 | Chronic pathology and tissue sequelae after IAV infection mimics features of human PASC-PF. (a) Representative immunofluorescence images staining CD8+ T cells (CD8α+) and epithelial progenitors (KRT5+ and KRT8high), and **(b)** quantification of KRT5+ area in young and aged lungs post IAV infection (n = 4-11 per time point) (*p = 0.0257). **(c)** Representative immunofluorescence images and **(d)** quantification of KRT8high transitional cells expressing PDLIM7 in young and aged C57BL/6 mouse lungs post-IAV infection (42 d.p.i.; n = 4) (*p = 0.0332). **(e)** Scatter plot comparing gene expression profiles of KRT8high transitional cells in young and aged mice following 14 days post-bleomycin injury from a previously published dataset (GSE157995). **(f)** Representative H&E and MT images (Scale bar – black = 500 μm; grey = 2 mm) and **(g)** evaluation of fibrotic disease (****p < 0.0001), and **(h)** evaluation of pathological lesions (**p = 0.0023, 0.0027; ****p < 0.0001) in aged naïve and IAV-infected C57BL/6 mice (250 d.p.i.) (n = 3 naïve, 8 infected). **(i)** Quantification of CD8+ T cells (*p = 0.0458), **(j)** KRT8high (*p = 0.0458), **(k)** KRT5+ areas (*p = 0.0327), **(l)** PDPN+ AT1 cells (*p = 0.0305) and **(m)** proSP-C+ AT2 cells in naïve and IAV-infected (250 d.p.i.) aged C57BL/6 mouse lungs (n = 3 naïve, 8 infected). Data are representative of two (**d,g-m**) or three (**b**) independent experiments. Statistical analyses were conducted using a two-tailed unpaired t-test (**d,g,i-m**), and two-way ANOVA (**b,h**). *p < 0.05; **p < 0.01; ***p < 0.001; ****p < 0.0001. Data are expressed as mean ± SEM; ns – not significant.

Extended Data Fig. 5 | See next page for caption.

Extended Data Fig. 5 | IAV infection of aged mice induces a sustained loss of alveolar epithelial cells unlike SARS-CoV-2. (a) Representative immunofluorescence images of aged C57BL/6 and BALB/c mouse lungs infected with SARS-CoV-2 MA-10, staining alveolar epithelial cell markers (AT1- PDPN; AT2 – proSP-C). **(b)** Quantification of proSP-C$^+$ AT2 (*p = 0.0141, 0.0168) and **(c)** PDPN$^+$ AT1 area in aged C57BL/6 mice following SARS-CoV-2 MA-10 infection (n = 3-4 per time point). **(d)** Quantification of proSP-C$^+$ AT2 (***p = 0.0005) and **(e)** PDPN$^+$ AT1 area in aged BALB/c mice following SARS-CoV-2 MA-10 infection (n = 3-4 per time point). **(f)** Representative immunofluorescence images, and **(g-i)** quantification of proSP-C$^+$ AT2 (Young - *p = 0.0333; **p = 0.0070. Aged - *p = 0.0391; **p = 0.0037; ***p = 0.0002) and PDPN$^+$ AT1 (Young - **p = 0.0020, 0.0012; ***p = 0.0002. Aged - *p = 0.0441; **p = 0.0068) area in young and aged C57BL/6 mice following IAV infection (n = 3-4 per time point). **(j)** Representative immunofluorescence images of aged C57BL/6 mouse lungs infected with IAV or SARS-CoV-2 virus, staining for AT1 cells (PDPN) and viral nucleoprotein (NP). **(k)** Schematic of the FlexiVent system to evaluate pulmonary function in mice. The diagram was created using BioRender. **(l)** Evaluation of compliance of the respiratory system in young and aged mice post PBS administration or IAV infection (60 d.p.i.) (n = 3 per time point) (*p = 0.0135; **p = 0.0034). Data are representative of two (**b-e,l**) or three (**g-h**) independent experiments. Statistical analyses were conducted using a one-way ANOVA (**b-e,h,i,l**) and two-way ANOVA (**g**). *p < 0.05; **p < 0.01; ***p < 0.001. Data are expressed as mean ± SEM; ns – not significant.
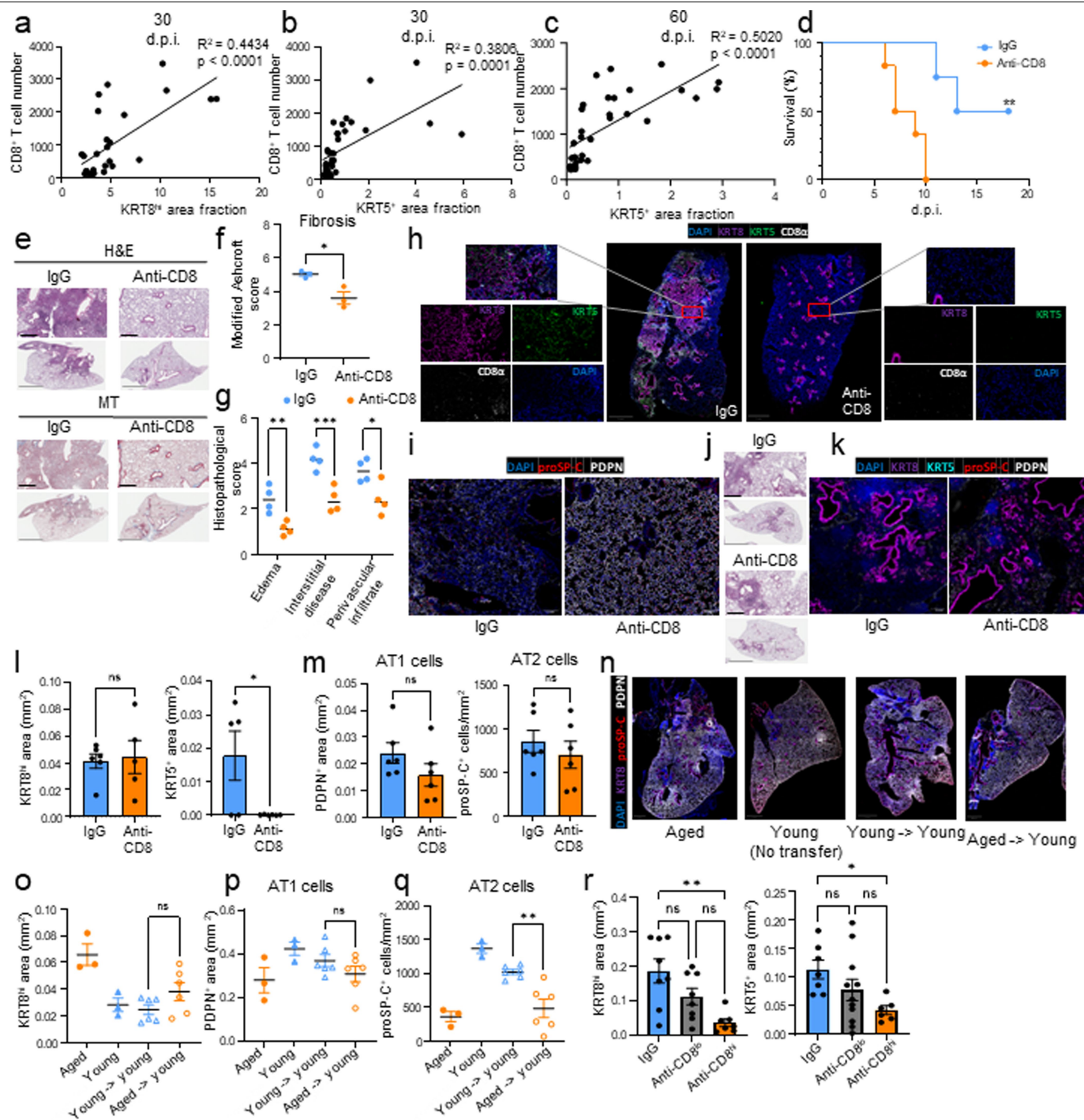
Extended Data Fig. 6 | Depletion of lung-resident CD8⁺ T cells improves fibrotic disease in aged but not young mice. (a) Simple linear regression of CD8⁺ T cell number and KRT8^high or **(b)** KRT5⁺ area fraction in aged IAV-infected mouse lungs at 30 d.p.i. (5-7 random fields/lung; n = 5) and **(c)** 60 d.p.i. (5-7 random fields/lung; n = 5). **(d)** Survival data of aged IAV-infected C57BL/6 mice following CD8⁺ T cell depletion prior to infection (n = 4 control IgG, 6 anti-CD8) (**p = 0.0046). **(e)** Representative H&E and MT images and **(f)** evaluation of fibrotic disease (n = 3 control IgG, 3 anti-CD8) (*p = 0.0207), and **(g)** pathological lesions in aged IAV-infected C57BL/6 mice (60 d.p.i.) following treatment with anti-CD8 or control IgG Ab. (n = 4 control IgG, 4 anti-CD8) (*p = 0.0125; **p = 0.0094; ***p = 0.0006). **(h)** Representative immunofluorescence images staining CD8⁺ T cells (CD8α⁺) and epithelial progenitors (KRT5⁺ and KRT8^high), and **(i)** AT1 (PDPN⁺) and AT2 (proSP-C⁺) in aged C57BL/6 mouse lungs post IAV infection (60 d.p.i.), treated with anti-CD8 or control IgG Ab. **(j)** Representative H&E images **(k)** and immunofluorescence images of young C57BL/6 lungs post IAV infection (60 d.p.i.) treated with anti-CD8 or control IgG Ab. **(l)** Quantification

of KRT8^high, KRT5⁺ (*p = 0.0255), **(m)** AT1, and AT2 cells in young IAV-infected mouse lungs, treated with anti-CD8 Ab or control IgG Ab. (n = 5-6 IgG, 5-6 anti-CD8). **(n)** Representative immunofluorescence images of aged and young C57BL/6 lungs post-IAV infection (42 d.p.i.) following receipt of lung CD8⁺ T cells from young or aged infection-matched donors at 21 d.p.i. **(o)** Quantification of KRT8^high area, **(p)** AT1 and **(q)** AT2 cells (**p = 0.0035) in aged or young C57BL/6 lungs post-IAV infection (42 d.p.i.) following receipt of lung CD8⁺ T cells from young or aged infection-matched donors at 21 d.p.i. (n = 3-6 per group). **(r)** Quantification of KRT8^high (**p = 0.0021) and KRT5⁺ area (*p = 0.0454) in aged IAV-infected mouse lungs (60 d.p.i.), treated with control IgG Ab, low dose anti-CD8 or high dose anti-CD8 (n = 6-11 per group). Scale bar – black = 500 μm; grey = 2 mm. Data are representative of two (**d,f,g,o**) or three (**l,m,r**) independent experiments. Statistical analyses were conducted using a two-tailed unpaired t-test (**f,l,m**), two-way ANOVA (**g**), and an ordinary one-way ANOVA (**o-r**). *p < 0.05; **p < 0.01; ***p < 0.001. Data are expressed as mean ± SEM; ns – not significant.
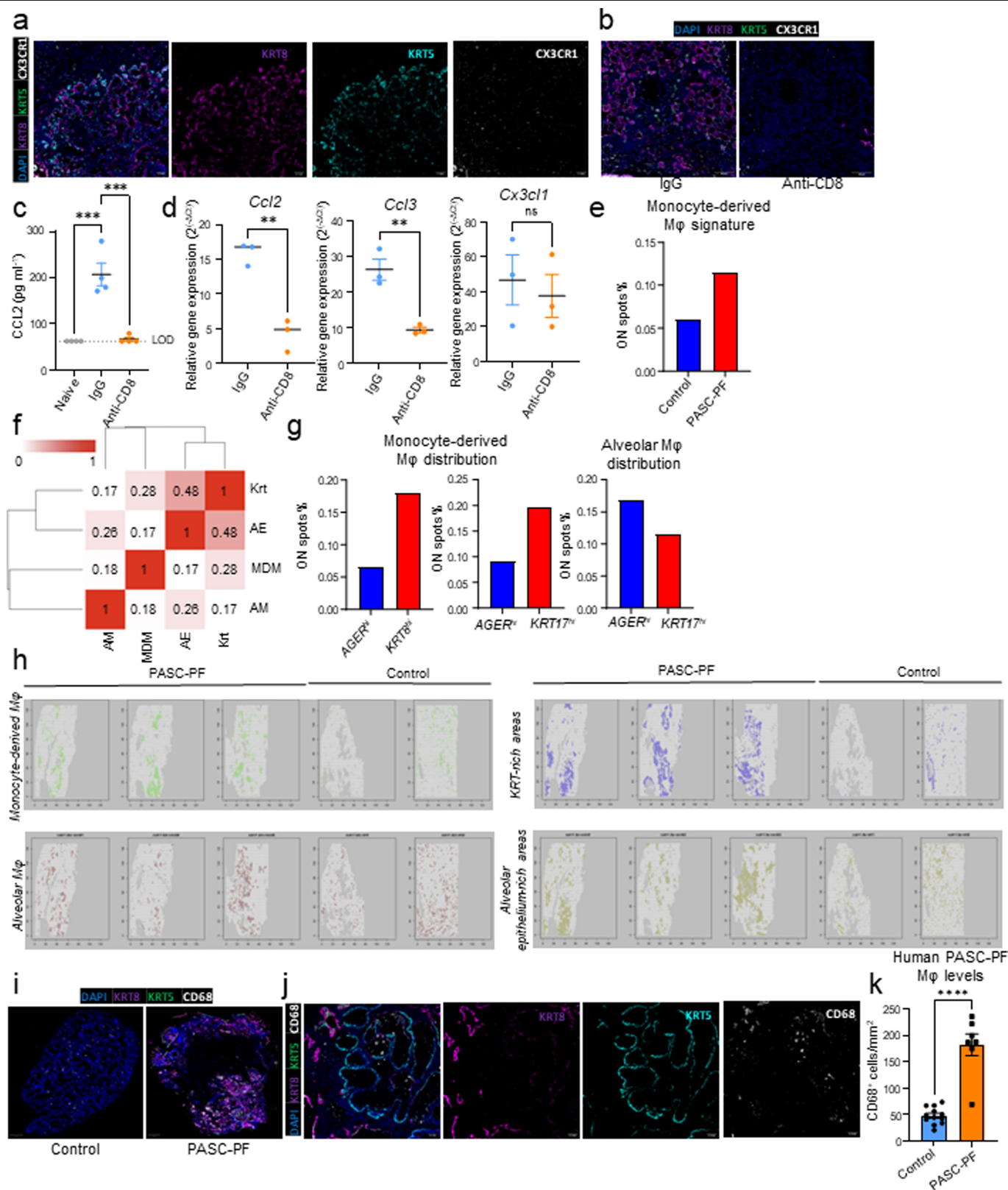
a Control Anti-CD8

b cluster

c AT1 / AT2 / Krt5 / Krt8 / CD8 / IM/MDM

d Human PASC-PF DEGs
Avg. Exp
Krt AE
Mouse IAV
p=2.5441e-06

e Human Krt-areas DEGs
Avg. Exp
Krt AE
Mouse IAV
p=3.0204e-31

f Human PASC-PF pathways
Avg. Exp
Krt AE
Mouse IAV
p=5.8696e-05

g Human PASC-PF DEGs
Avg. Exp
IgG Anti-CD8
Mouse IAV
p=2.0300e-05

h Human Krt-areas DEGs
Avg. Exp
IgG Anti-CD8
Mouse IAV19
p=1.1986e-19

i Human PASC-PF pathways
Avg. Exp
IgG Anti-CD8
Mouse IAV
p=7.7334e-04

j Krt vs AE
GSEA Results
RESPONSE_TO_GROWTH_FACTOR
BLOOD_VESSEL_MORPHOGENESIS
VASCULATURE_DEVELOPMENT
ANGIOGENESIS
VASCULAR_PROCESS_IN_CIRCULATORY_SYSTEM
TRANSMEMBRANE_RECEPTOR_PROTEIN_SERINE_THREONINE_KINASE_SIGNALING_PATHWAY
VASCULOGENESIS
CIRCULATORY_SYSTEM_PROCESS
CELL_JUNCTION_ASSEMBLY
TUBE_MORPHOGENESIS
DEFENSE_RESPONSE
IMMUNE_RESPONSE
BIOLOGICAL_PROCESS_INVOLVED_IN_SYMBIOTIC_INTERACTION
BIOLOGICAL_PROCESS_INVOLVED_IN_INTERSPECIES_INTERACTION_BETWEEN_ORGANISMS
RESPONSE_TO_BACTERIUM
DEFENSE_RESPONSE_TO_OTHER_ORGANISM
INNATE_IMMUNE_RESPONSE
ANTIMICROBIAL_HUMORAL_RESPONSE
HUMORAL_IMMUNE_RESPONSE
DEFENSE_RESPONSE_TO_BACTERIUM
Normalized Enrichment Score (NES)
Enrichment Score
-log10 adjusted p-value

k ADI/DATP/PATS
Mean normalized gene exp
Krt AE
p=1e-300

Aberrant basaloid
Mean normalized gene exp
Krt AE
p=1.0218e-49

l Dysplastic epithelial progenitors
IgG / Anti-CD8 — Krt8
IgG / Anti-CD8 — Krt5
IgG / Anti-CD8 — Trp63

m Alveolar epithelial cells
IgG / Anti-CD8 — Sftpc
IgG / Anti-CD8 — Ager
IgG / Anti-CD8 — Sftpa1

n CD8+ T cells
IgG / Anti-CD8 — CD8a
IgG / Anti-CD8 — CD8b1
IgG / Anti-CD8 — Itgae

o Monocyte-derived macrophages
IgG / Anti-CD8 — Cx3cr1
IgG / Anti-CD8 — Cd14
IgG / Anti-CD8 — S100a6

p Alveolar macrophages
IgG / Anti-CD8 — Flt1
IgG / Anti-CD8 — Car4
IgG / Anti-CD8 — Fabp5

q Fibrosis
IgG / Anti-CD8

Extended Data Fig. 7 | See next page for caption.

Article

a

b

c

d

e
Monocyte-derived
Mφ signature

f

g
Monocyte-derived
Mφ distribution

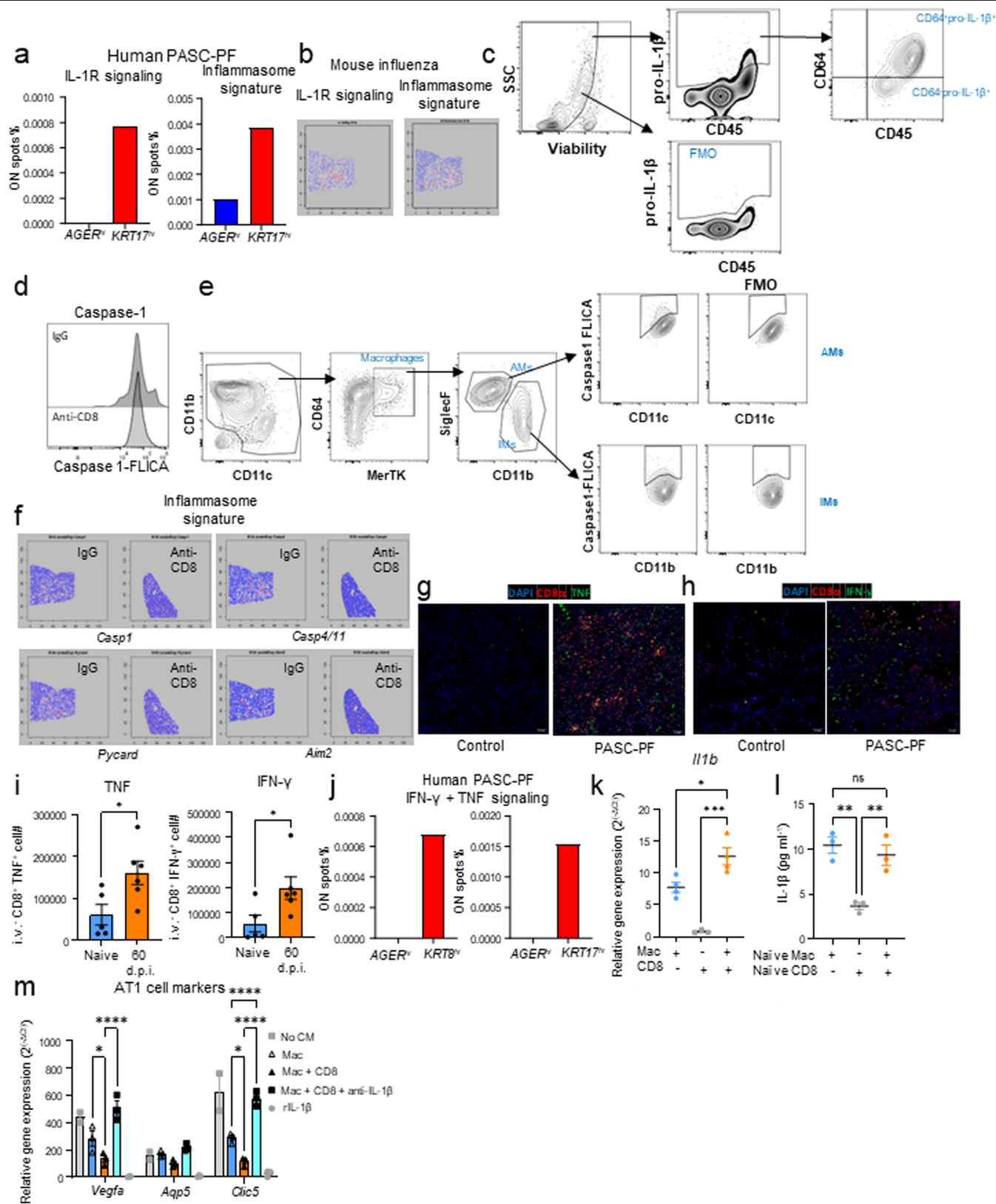Alveolar Mφ
distribution

h

i

j

k
Human PASC-PF
Mφ levels

Extended Data Fig. 8 | See next page for caption.

Extended Data Fig. 8 | Monocyte-derived macrophages but not alveolar macrophages are enriched in areas of dysplastic repair within human and mouse post-viral lungs. (a) Representative immunofluorescence image of aged IAV-infected C57BL/6 mouse lungs staining for CXC3CR1[+] macrophages and dysplastic progenitors (KRT5 and KRT8). (b) Representative immunofluorescence images of aged IAV-infected (60 d.p.i.) lungs treated with control IgG Ab or anti-CD8, staining monocyte-derived macrophages (CX3CR1) and dysplastic epithelial progenitors (KRT5 and KRT8). (c) Evaluation of CCL2 levels in bronchoalveolar lavage fluid from naïve or aged IAV-infected mice treated with control IgG Ab or anti-CD8 (n = 4 per group) (***p = 0.0002). (d) Quantification of *Ccl2* (**p = 0.0020), *Ccl3* (**p = 0.0052)*,* and *Cx3cl1* gene expression in lungs of aged IAV-infected mice treated with control IgG Ab or anti-CD8 (n = 3 IgG, 3 αCD8). (e) Quantification of the proportion of spots expressing the gene signature of monocyte-derived macrophages in human control and PASC-PF lungs. (f) Heatmap of the physical distribution of monocyte-derived macrophages (MDM), alveolar macrophages (AM), healthy alveolar epithelium (AE), and dysplastic areas (Krt) within human PASC-PF lungs. (g) Quantification of the proportion of spots expressing gene signatures characterizing monocyte-derived macrophages and alveolar macrophages in *AGER*[hi] and *KRT17*^{hi} areas of human PASC-PF (n = 3) lungs. (h) Spatial gene expression maps of monocyte-derived macrophages, Krt-rich dysplastic areas, alveolar macrophages and healthy alveolar epithelium in human control (n = 2) and PASC-PF (n = 3) lungs. (i) Representative immunofluorescence image of human PASC-PF lungs staining for CD68^{+} macrophages and dysplastic progenitors (KRT5 and KRT8). (k) Quantification of CD68^{+} macrophages in human control and PASC-PF lungs (n = 12 control; 7 PASC-PF) (****p < 0.0001). Data are representative of two (c,d) independent experiments. Statistical analyses were conducted using a two-tailed unpaired t-test (d,k), and an ordinary one-way ANOVA (c). **p < 0.01; ***p < 0.001; ****p < 0.0001. Data are expressed as mean ± SEM; ns – not significant.
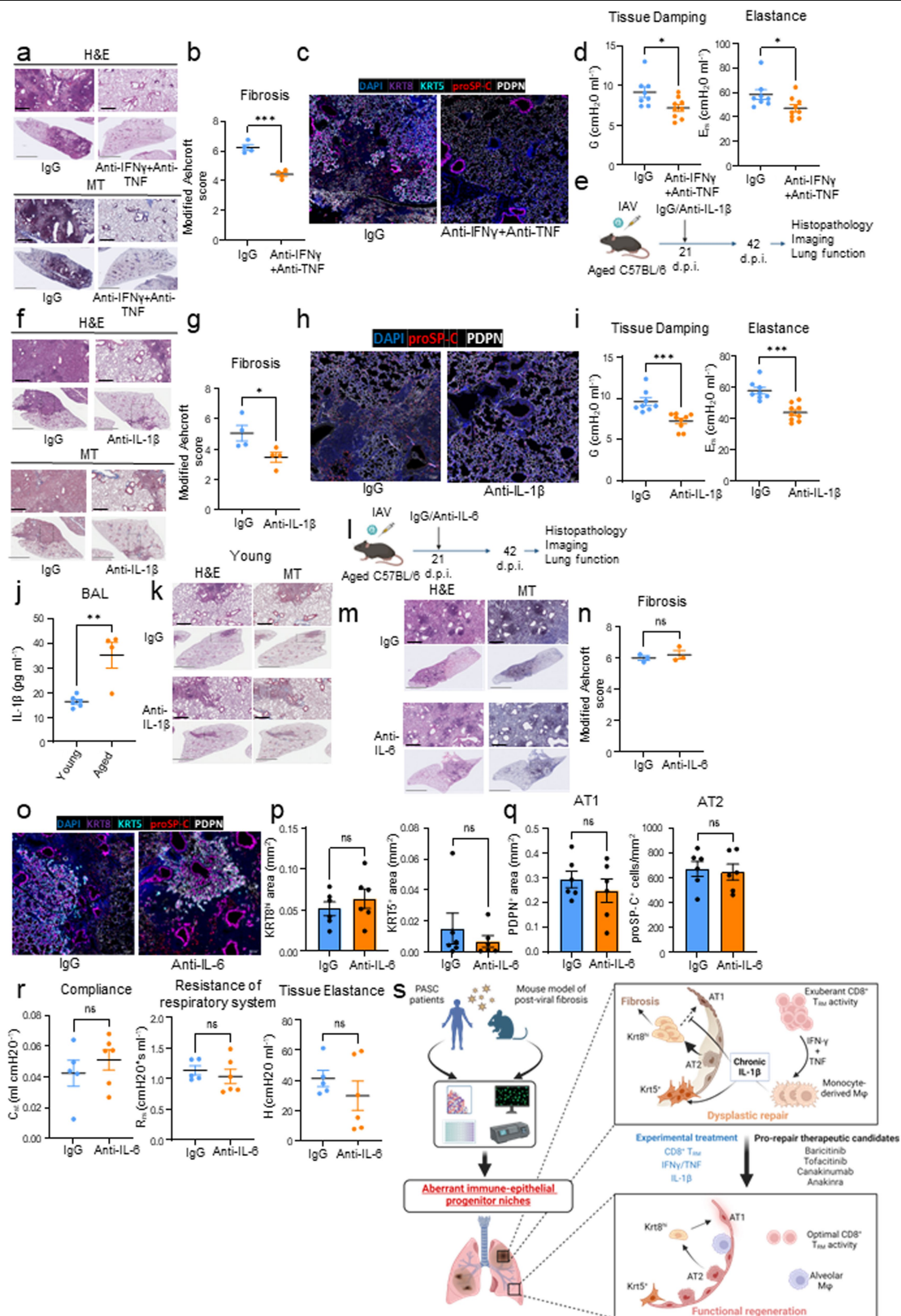
a Human PASC-PF
IL-1R signaling

b Mouse influenza
IL-1R signaling   Inflammasome signature

c

d Caspase-1

e

f Inflammasome signature

g DAPI CD8α TNF
Control   PASC-PF

h DAPI CD8α IFN-γ
Control   PASC-PF

i TNF   IFN-γ

j Human PASC-PF
IFN-γ + TNF signaling

k *Il1b*

l

m AT1 cell markers

Extended Data Fig. 9 | See next page for caption.

Article

Extended Data Fig. 9 | Areas of dysplastic repair are enriched with IL-1R signalling and inflammasome signatures in human PASC-PF and aged IAV-infected mouse lungs. (a) Proportions of spots expressing gene signatures of IL-1R signalling and inflammasome activity in $AGER^{hi}$ and $KRT17^{hi}$ areas of human PASC-PF lungs. **(b)** Spatial gene expression maps of IL-1R signalling and inflammasome activity in aged IAV-infected mouse lungs (60 d.p.i.). **(c)** Gating strategy to identify proIL-1β⁺ cells IAV-infected mouse lungs by flow cytometry. **(d)** Histograms of caspase-1 levels in lungs of aged IAV-infected mice treated with IgG or Anti-CD8. **(e)** Gating strategy to identify FLICA⁺ cells in IAV-infected mice. **(f)** Spatial gene expression maps of inflammasome components in aged IAV-infected mice (60 d.p.i.) treated with IgG Ab or anti-CD8. **(g)** Representative immunofluorescence images staining for CD8⁺ T cells (CD8α) and TNF, and **(h)** IFN-γ in human control and PASC-PF lungs. **(i)** Quantification of TNF⁺ (*p = 0.0266) and IFN-γ⁺ (*p = 0.0378) lung-resident CD8⁺ T cells in naïve and IAV-infected (60 d.p.i.) aged mouse lungs (n = 5 naïve, 6 infected). **(j)** Proportions of spots expressing gene signatures of IFN-γ + TNF signalling in healthy ($AGER^{hi}$) and diseased areas ($KRT8^{hi}$ or $KRT17^+$) within human PASC-PF (n = 3) lungs. **(k)** Quantification of IL-1β gene expression (n = 3-4 wells/condition pooled from 4 mice) (*p = 0.0174; ***p = 0.0001), and **(l)** evaluation of IL-1β release following coculture of macrophages and CD8⁺ T cells from naïve aged C57BL/6 mice (n = 3 wells/ condition pooled from 4 mice) (**p = 0.0037, 0.0089). **(m)** Gene expression of AT1 cell markers 3 days post AT2 cell culture and exposure to conditioned media (CM) (n = 2-3 wells/condition pooled from 5 mice) (*p = 0.0119, 0.0395; ****p < 0.0001). Data are representative of two (**i,k,l,m**) independent experiments. Statistical analyses were conducted using a two-tailed unpaired t-test (**i**), an ordinary one-way ANOVA (**k,l**), and a two-way ANOVA (**m**). *p < 0.05; **p < 0.01; *** p < 0.001; ****p < 0.0001. Data are expressed as mean ± SEM; ns – not significant.

Article

Corresponding author(s): Jie Sun

Last updated by author(s): 07/12/2024

Reporting Summary

Nature Portfolio wishes to improve the reproducibility of the work that we publish. This form provides structure for consistency and transparency in reporting. For further information on Nature Portfolio policies, see our Editorial Policies and the Editorial Policy Checklist.

Statistics

For all statistical analyses, confirm that the following items are present in the figure legend, table legend, main text, or Methods section.

n/a	Confirmed	
☐	☒	The exact sample size (*n*) for each experimental group/condition, given as a discrete number and unit of measurement
☐	☒	A statement on whether measurements were taken from distinct samples or whether the same sample was measured repeatedly
☐	☒	The statistical test(s) used AND whether they are one- or two-sided *Only common tests should be described solely by name; describe more complex techniques in the Methods section.*
☒	☐	A description of all covariates tested
☐	☒	A description of any assumptions or corrections, such as tests of normality and adjustment for multiple comparisons
☐	☒	A full description of the statistical parameters including central tendency (e.g. means) or other basic estimates (e.g. regression coefficient) AND variation (e.g. standard deviation) or associated estimates of uncertainty (e.g. confidence intervals)
☐	☒	For null hypothesis testing, the test statistic (e.g. *F*, *t*, *r*) with confidence intervals, effect sizes, degrees of freedom and *P* value noted *Give P values as exact values whenever suitable.*
☒	☐	For Bayesian analysis, information on the choice of priors and Markov chain Monte Carlo settings
☒	☐	For hierarchical and complex designs, identification of the appropriate level for tests and full reporting of outcomes
☒	☐	Estimates of effect sizes (e.g. Cohen's *d*, Pearson's *r*), indicating how they were calculated

Our web collection on statistics for biologists contains articles on many of the points above.

Software and code

Policy information about availability of computer code

Data collection	Flow cytometry: Attune NXT software (v5.2.0); Microscopy: cellSens; Spatial Transcriptomics: 10X Visium spaceranger (v2.0, genome version mm10)
Data analysis	Flow cytometry: FlowJo; Microscopy: QuPath, ImageJ FIJI; Spatial transcriptomics: R Seurat (v4.3.0) for basic analyses. SCTransform method (v0.3.5) for normalization. Harmony (v0.1) for batch correction; Statistical analyses: GraphPad Prism

For manuscripts utilizing custom algorithms or software that are central to the research but not yet described in published literature, software must be made available to editors and reviewers. We strongly encourage code deposition in a community repository (e.g. GitHub). See the Nature Portfolio guidelines for submitting code & software for further information.

Data

Policy information about availability of data

All manuscripts must include a data availability statement. This statement should provide the following information, where applicable:
- Accession codes, unique identifiers, or web links for publicly available datasets
- A description of any restrictions on data availability
- For clinical datasets or third party data, please ensure that the statement adheres to our policy

All raw and processed spatial transcriptomics data have been uploaded to GEO database (GSE267227 and GSE267228). Relevant code used for analysis of spatial transcriptomics data has been deposited at github (https://github.com/zang-lab/covidSTanalysis) or available online - genome version mm10.

Research involving human participants, their data, or biological material

Policy information about studies with human participants or human data. See also policy information about sex, gender (identity/presentation), and sexual orientation and race, ethnicity and racism.

Reporting on sex and gender	We have included information regarding the biological sex of patient cohorts in the supplementary table 1. Gender information was not available (M=13, F=5; Cohort size = 18 in the Cedars Sinai cohort, information of the UVA cohort is not available)
Reporting on race, ethnicity, or other socially relevant groupings	N/A
Population characteristics	Autopsy lung samples from influenza or COVID-19 patients; or from organ donors (prior influenza infection - Lifelink of Georgia); Patients with advanced stage lung fibrosis following COVID-19 required lung transplantation. Age (25-79) of patient cohort has been described in Supplementary information.
Recruitment	Patients were enrolled into IRB-approved Biobank studies at Cedars-Sinai Medical Center or University of Virginia Health Systems.
Ethics oversight	Approved by IRB committee at Cedars Sinai or University of Virginia; Prior-influenza samples exempt from IRB review as donors were deceased at time of collection. Informed consent obtained from next of kin before explant.

Note that full information on the approval of the study protocol must also be provided in the manuscript.

Field-specific reporting

Please select the one below that is the best fit for your research. If you are not sure, read the appropriate sections before making your selection.

☒ Life sciences   ☐ Behavioural & social sciences   ☐ Ecological, evolutionary & environmental sciences

For a reference copy of the document with all sections, see nature.com/documents/nr-reporting-summary-flat.pdf

Life sciences study design

All studies must disclose on these points even when the disclosure is negative.

Sample size	Sample size was chosen based on previous experience in our group as well as published studies with similar layout
Data exclusions	No data was excluded from analyses
Replication	All data were replicated over at least two independent experiments
Randomization	Experimental groups were randomly allocated
Blinding	Data were not blinded as the same investigators performed the experiments and analyzed results

Reporting for specific materials, systems and methods

We require information from authors about some types of materials, experimental systems and methods used in many studies. Here, indicate whether each material, system or method listed is relevant to your study. If you are not sure if a list item applies to your research, read the appropriate section before selecting a response.

Materials & experimental systems

n/a	Involved in the study
☐	☒ Antibodies
☐	☒ Eukaryotic cell lines
☒	☐ Palaeontology and archaeology
☐	☒ Animals and other organisms
☒	☐ Clinical data
☒	☐ Dual use research of concern
☒	☐ Plants

Methods

n/a	Involved in the study
☒	☐ ChIP-seq
☐	☒ Flow cytometry
☒	☐ MRI-based neuroimaging

Antibodies

Antibodies used	All antibodies used in the study were obtained from commercial suppliers. All relevant information is provided in supplementary table and also listed here:

Immunofluorescence
Rat anti-cytokeratin 8 (TROMA-1) DSHB Antibody Registry ID: AB 531826
Rabbit anti-proSP-C Millipore Sigma Cat#: AB3786
Hamster anti-PDPN Abcam Cat#: ab11936
Chicken anti-cytokeratin 5 (human) BioLegend Cat#: 905901
Chicken anti-cytokeratin 5 (mouse) BioLegend Cat#: 905903
Rabbit anti-CD8α (human) Cell Signaling Technologies Cat#: 85336S
Rabbit anti-CD8α (mouse) Cell Signaling Technologies Cat#: 98941S
Rabbit anti-cytokeratin 17 Millipore Sigma Cat#: HPA000453
Mouse anti-SMA Millipore Sigma Cat#: A5528
Rabbit anti-AGER Proteintech
 Cat#: 16346-1-AP
Mouse anti-CD68 Abcam Cat#: Ab955
Mouse anti-proSP-C Santa Cruz Cat#: sc-518029
Rabbit anti-CX3CR1 ThermoFisher Cat#: 14-6093-81
Mouse anti-TNF Abcam Cat#: ab1793
Rabbit anti-IFNγ Proteintech Cat#: 15365-1-AP
Rabbit anti-Influenza A virus NP GeneTex Cat#: GTX125989
Rabbit anti-SARS-CoV-2 NP GeneTex Cat#: GTX135357
Rabbit anti-PDLIM7 Novus Biologicals Cat#: NPB1-84841
DyLight 649 Donkey anti-rabbit IgG BioLegend Cat#: 406406
Donkey anti-chicken IgGY (H+L) Alexa Fluor 488 IgG (H+L) ThermoFisher Cat#: A78948

Goat anti-rat IgG (H+L) Alexa Fluor 555 ThermoFisher Cat#: A48270
Goat anti-Armenian Hamster IgG (H+L) Alexa Fluor 488 ThermoFisher Cat#: A78963
Goat anti-Chicken IgY (H&L) Alexa Fluor 750 Abcam Cat#: ab175755
Goat anti-rat IgG (H+L) Alexa Fluor 488 ThermoFisher Cat#: A-11006
Goat anti-rabbit IgG (H+L) Alexa Fluor 488 ThermoFisher Cat#: A-11008

Antibodies (Flow cytometry)
Viability dye (Zombie NIR) BioLegend Cat#: 423105
Viability dye (Zombie Aqua) BioLegend Cat#: 423101
CD8a-BV510 (53-6.7) BioLegend Cat#: 100751
CD11b-BV510 (M1/70) BioLegend Cat#: 101245
CD11b-PerCP/Cy5.5 (M1/70) BioLegend Cat#: 101227
CD11c-BV421 (N418) BioLegend Cat#: 117329
CD45-BV605 (30-F11) BioLegend Cat#: 103139
CD64-BV711 (X54-5/7.1) BioLegend Cat#: 139311
IA/IE−PerCP/Cy5.5 (M5/114.15.2) BD Biosciences Cat#: 556999
IL-1b-PE (NJTEN3) eBioscience Cat#: 12-7114-82
Ly6C-PE (HK1.4) BioLegend Cat#: 128007
Ly6G-PE/Cy7 (1A8) BioLegend Cat#: 127617
MerTK-APC (2B10C42) BioLegend Cat#: 151507
Influenza NP366-374-APC NIH IEDB ID: 4602
SiglecF-APC/Cy7 (E50-2440) BD Biosceinces Cat#: 155531
CD45-APC (30-F11) BioLegend Cat#: 103111
EpCAM/CD326 − PerCP/Cy5.5 (G8.8) BioLegend Cat#: 118219
IA/IE-FITC (M5/114.15.2) BioLegend Cat#: 107605

Validation	All antibodies were validated by suppliers as described below:

 Rat anti-cytokeratin 8 (TROMA-1) TROMA-I specificity for keratin K8 has been knock-out validated. See PMID: 27234655.
 Rabbit anti-proSP-C Immunohistochemistry (Paraffin) Analysis: A 1:2,000 dilution from a representative lot detected Prosurfactant Protein C (proSP-C) in mouse lung tissue sections.
 Hamster anti-PDPN Abpromise guarantee covers the use of ab11936 in the following tested applications - Immunofluorecence
 Chicken anti-cytokeratin 5 (human) Each lot of this antibody is quality control tested by immunohistochemical staining of formalin-fixed paraffin-embedded sections of human skin.
 Chicken anti-cytokeratin 5 (mouse) Each lot of this antibody is quality control tested by formalin-fixed paraffin-embedded immunohistochemical staining. For immunohistochemistry, a concentration range of $0.1 - 5.0$ µg/ml is suggested. It is recommended that the reagent be titrated for optimal performance for each application.
 Rabbit anti-CD8α (human)   this product has met all of the quality control standards defined by Cell Signaling Technology, Inc.
 Rabbit anti-CD8α (mouse)   this product has met all of the quality control standards defined by Cell Signaling Technology, Inc.
 Rabbit anti-cytokeratin 17 Enhanced validation by orthogonal RNAseq
 Mouse anti-SMA Enhanced validation by orthogonal RNAseq
 Rabbit anti-AGER KO validated. Positive IHC detected in mouse lung tissue, human lung tissue, human renal cell carcinoma tissue
 Mouse anti-CD68 Abpromise guarantee covers the use of ab955 in the following tested applications - Immunofluorecence
 Mouse anti-proSP-C Western blot analysis of SP-C expression in non-transfected (A) and human SP-C transfected (B) 293T whole cell

lysates.

Rabbit anti-CX3CR1 This Antibody was verified by Knockdown to ensure that the antibody binds to the antigen stated.

Mouse anti-TNF Abpromise guarantee covers the use of ab1793 in the following tested applications - Immunofluorecence

Rabbit anti-IFNγ KD/KO validated; positive WB detected in NK-92 cells recombinant protein

Rabbit anti-Influenza A virus NP Orthogonal validation by WB, IF and ELISA

Rabbit anti-SARS-CoV-2 NP   Orthogonal validation by WB, IF and ELISA

Rabbit anti-PDLIM7 Orthogonal validation by WB in human cellines U2OS and HEK293

Viability dye (Zombie NIR) One day old C57BL/6 mouse splenocytes were stained with Zombie NIR™ and analyzed before fixation (purple) or after fixation and permeabilization (red).

Viability dye (Zombie Aqua) One day old C57BL/6 mouse splenocytes were stained with Zombie NIR™ and analyzed before fixation (purple) or after fixation and permeabilization (red).

CD8a-BV510 (53-6.7) C57BL/6 mouse splenocytes were stained with CD3 APC and CD8a (clone 53-6.7) Brilliant Violet 510™.

CD11b-BV510 (M1/70) C57BL/6 mouse bone marrow cells were stained with CD11b (clone M1/70) Brilliant Violet 510™. Data shown was gated on the myeloid cell population

CD11b-PerCP/Cy5.5 (M1/70) C57BL/6 splenocytes were blocked with TruStain FcX™ (anti-mouse CD16/32) Antibody then stained with Ly-6G/Ly-6C (Gr-1) APC and CD11b (clone M1/70) PerCP/Cyanine5.5 (left) or rat IgG2b, κ PerCP/Cyanine5.5 isotype control (right).

CD11c-BV421 (N418) 57BL/6 mouse splenocytes were stained with mouse I-A/I-E FITC and CD11c (clone N418) Brilliant Violet 421™ (top) or Armenian hamster IgG Brilliant Violet 421™ isotype control (bottom).

CD45-BV605 (30-F11) C57BL/6 mouse splenocytes were stained with CD45 (clone 30-F11) Brilliant Violet 605™ (filled histogram) or rat IgG2b, κ Brilliant Violet 605™ isotype control (open histogram).

CD64-BV711 (X54-5/7.1) C57BL/6 mouse bone marrow cells were stained with CD11b FITC and CD64 (clone X54-5/7.1) Brilliant Violet 711™ (top) or mouse IgG1, κ Brilliant Violet 711™ isotype control (bottom).

IA/IE–PerCP/Cy5.5 (M5/114.15.2) This antibody is routinely tested by flow cytometric analysis. Ot

IL-1b-PE (NJTEN3) This Antibody was verified by Cell treatment to ensure that the antibody binds to the antigen stated.

Ly6C-PE (HK1.4) C57BL/6 bone marrow cells were stained with Ly-6C (clone HK1.4) PE (filled histogram), or rat IgG2c, κ PE isotype control (open histogram

Ly6G-PE/Cy7 (1A8) C57BL/6 bone marrow cells stained with 1A8 PE/Cyanine7

MerTK-APC (2B10C42) 57BL/6 mouse splenocytes were stained with CX3CR1 PE and MERTK (clone 2B10C42) APC (top) or rat IgG2a, κ APC isotype control (bottom).

Influenza NP366-374-APC IEDB_Reference:1313

SiglecF-APC/Cy7 (E50-2440) Two-color flow cytometric analysis of Siglec-F expression on mouse bone marrow cells

CD45-APC (30-F11) C57BL/6 mouse splenocytes stained with 30-F11 APC

EpCAM/CD326 – PerCP/Cy5.5 (G8.8) Mouse thymic epithelial stromal cell line (TE-71) stained with G8.8 PerCP/Cyanine5.5

IA/IE-FITC (M5/114.15.2) C57BL/6 mouse splenocytes were stained with anti-mouse I-A/I-E (clone M5/114.15.2)

Eukaryotic cell lines

Policy information about cell lines and Sex and Gender in Research

Cell line source(s)	Vero E6 cells were purchased from ATCC
Authentication	Cell lines were not independently authenticated beyond the identity provided by ATCC
Mycoplasma contamination	Cell lines tested negative for mycoplasma
Commonly misidentified lines (See ICLAC register)	None

Animals and other research organisms

Policy information about studies involving animals; ARRIVE guidelines recommended for reporting animal research, and Sex and Gender in Research

Laboratory animals	C57BL/6 (2-3mo old or 20-22mo old), BALB/c (10-12mo old) , and K18-hACE2 (10-12mo old) mice were utilized where indicated
Wild animals	No wild animals were used in the study
Reporting on sex	Studies were performed primarily in female mice due to long-term housing and aging
Field-collected samples	No field samples were collected in the study
Ethics oversight	Studies were approved by the IACUC at the Mayo Clinic or the University of Virginia

Note that full information on the approval of the study protocol must also be provided in the manuscript.

Plants

Seed stocks	*Report on the source of all seed stocks or other plant material used. If applicable, state the seed stock centre and catalogue number. If plant specimens were collected from the field, describe the collection location, date and sampling procedures.*
Novel plant genotypes	*Describe the methods by which all novel plant genotypes were produced. This includes those generated by transgenic approaches, gene editing, chemical/radiation-based mutagenesis and hybridization. For transgenic lines, describe the transformation method, the number of independent lines analyzed and the generation upon which experiments were performed. For gene-edited lines, describe the editor used, the endogenous sequence targeted for editing, the targeting guide RNA sequence (if applicable) and how the editor was applied.*
Authentication	*Describe any authentication procedures for each seed stock used or novel genotype generated. Describe any experiments used to assess the effect of a mutation and, where applicable, how potential secondary effects (e.g. second site T-DNA insertions, mosiacism, off-target gene editing) were examined.*

Flow Cytometry

Plots

Confirm that:

☒ The axis labels state the marker and fluorochrome used (e.g. CD4-FITC).

☒ The axis scales are clearly visible. Include numbers along axes only for bottom left plot of group (a 'group' is an analysis of identical markers).

☒ All plots are contour plots with outliers or pseudocolor plots.

☒ A numerical value for number of cells or percentage (with statistics) is provided.

Methodology

Sample preparation	Detailed methodology of sample preparation and processing is provided in methods section
Instrument	Attune NxT Flow cytometer
Software	Attune cytometric software
Cell population abundance	Frequency and total cell numbers are indicated in respective figures
Gating strategy	Detailed gating strategy provided in supplementary figures

☒ Tick this box to confirm that a figure exemplifying the gating strategy is provided in the Supplementary Information.